Journal of Cleaner Production 442 (2024) 141006

Contents lists available at ScienceDirect

Journal of Cleaner Production

journal homepage: www.elsevier.com/locate/jclepro

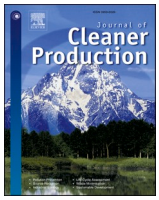

Triaxial compressive performance of recycled aggregate/glass sand concrete: Experimental study and mechanism analysis

Hanbing Zhao [a], Yong Hu [b,c,**], Yunan Li [b], Kejin Wang [d], Frank Dehn [e], Wengui Li [e,f,*]

[a] School of Civil and Environmental Engineering, University of Technology Sydney, NSW, 2007, Australia
[b] Faculty of Engineering, China University of Geosciences, Wuhan, Hubei, 430074, China
[c] Department of Civil Engineering, Wenhua College, Wuhan, Hubei 430074, China
[d] Department of Civil, Construction and Environmental Engineering, Iowa State University, IA, 50011, USA
[e] Institute of Concrete Structures and Building Materials (IMB), Karlsruhe Institute of Technology (KIT), DE-76131, Karlsruhe, Germany
[f] Centre for Infrastructure Engineering and Safety, School of Civil and Environmental Engineering, The University of New South Wales, NSW, 2052, Australia

ARTICLE INFO

Handling Editor: Zhen Leng

Keywords:
Recycled aggregate concrete
Recycled glass sand
Interfacial transition zone
Triaxial compression
Pore water pressure
Stress-strain curve

ABSTRACT

In real-world applications, concrete is often subjected to triaxial compression combined with pore water pressure. Understanding the mechanical properties of the concrete made with recycled coarse aggregate (RCA) and recycled glass sand (RGS) under complex stress states can enhance its practical application. This study first investigated the microscopic properties of interfacial transition zones (ITZs) using nanoscratch and backscattered electron-based (BSE-based) image analysis. Subsequently, mechanical properties under confining pressures ranging from 0 to 14 MPa and pore water pressure ranging from 0 to 13 MPa were assessed based on the stress-strain behaviours. The results reveal that the chemical activity and specific surface areas of aggregate were closely related to ITZ microscopic properties. Despite with the same water-cement ratio, the ITZs between RCA and the paste matrix displayed better cohesion performance than the ITZs between RGS and the paste matrix. Confining pressure was found to increase the internal friction angle of concrete, thereby improving mechanical strength and ductility. The poor cohesion of the RGS-paste matrix interface resulted in a decrease in the peak stress and an increase in the peak strain under triaxial compression. Pore water pressure played a dual role in triaxial compression, providing support and promoting crack expansion. The supporting effect enhanced the initial stiffness of concrete, while the crack expansion effect reduced the peak stress. The William-Warnke failure criterion was proven to be suitable for describing the failure surfaces of concrete with RCA and RGS under various complex stress states. To accurately predict the stress-strain curve, it is essential to comprehensively consider the influence of ITZs in concrete and the effect of pore water pressure.

1. Introduction

In concrete, coarse and fine aggregates with different sizes may account for 60–75 % of the total volume (Wang et al., 2021). Crushed natural rocks and river sand are generally considered as satisfying aggregates in concrete, and they are non-renewable natural resources. The development of urbanisation in recent years has prompted a surge in demand for concrete raw materials (Tang et al., 2020a; Zhang et al., 2023; Jiang et al., 2023a). According to some reports, excessive mining of natural sand and gravel in some cities has caused soil erosion, dike breach, river migration, etc (Lu et al., 2020). In addition, natural sand and stone are generally located in suburbs far away from a city. Long-distance transportation undoubtedly increases the consumption of fossil fuels, and it is not conducive to the global carbon reduction strategy (Li et al., 2023). On the other hand, there are waste materials such as waste crushed concrete and glass cullet in cities that can be recycled to replace traditional sand and gravel (Lu et al., 2019). Recycling these waste materials and developing green and sustainable concrete materials should receive more attention.

Crushed waste concrete and glass cullet can be recycled and reused as coarse and fine aggregate respectively in new concrete constructions, namely recycled coarse aggregate (RCA) and recycled glass sand (RGS)

* Corresponding author: Centre for Infrastructure Engineering and Safety, School of Civil and Environmental Engineering, The University of New South Wales, NSW, 2052, Australia.
** Corresponding author.
E-mail addresses: yonghu1210@yahoo.com (Y. Hu), wengui.li@unsw.edu.au (W. Li).

https://doi.org/10.1016/j.jclepro.2024.141006
Received 1 November 2023; Received in revised form 4 January 2024; Accepted 28 January 2024
Available online 3 February 2024

Fig. 1. Coarse and fine aggregate for preparing concrete specimens.

(Ye et al., 2022). To understand the performance of sustainable concrete mixed with RCA and RGS, it is necessary to explore the constituent distribution and micromechanical properties within interfacial transition zone (ITZ) between aggregate and cement paste matrix, because ITZ is generally the weakest region in concrete, which determines the mechanical properties and durability of concrete (Yue et al., 2020; Jiang et al., 2022).

Backscattered electron (BSE) images analysis technique is usually used to quantitatively characterise the constituents of cement-based materials (Kim et al., 2019). Pores, cracks, hydration products and unhydrated clinkers in BSE images can be segmented and statistically analysed according to grey level thresholds (Lyu et al., 2019a). In RCA, a layer of old mortar is often attached to the surface of natural coarse aggregate (NCA), thus existing old ITZs (between NCA and old paste matrix). After mixing with new cement paste, the weak regions between old and new paste matrix are called new ITZs. The different surface morphologies and chemical activity of natural sand, old cement paste and RGS lead to differences in the microscopic performance of the ITZs (Head and Buenfeld, 2006). In Djerbi (2018) research, image analysis was performed to quantify pores and unhydrated clinkers in the new ITZ of recycled aggregate concrete (RAC). The results show that the new ITZ in RAC has a higher porosity and lower proportion of unhydrated clinkers than natural aggregate concrete (NAC) (Djerbi, 2018). Kim et al. (2019) segmented pores in ITZs of RAC and image analysis showed that bonded mortar resulted in higher porosity in ITZs and thereby affected the concrete strength. In comparison, few studies use BSE-based image analysis technique to observe the phases of ITZ between RGS and new cement paste.

Luo et al. (2018, 2019), systematically summarised the micromechanical properties characterisation techniques of ITZs, including modulus mapping, grid nanoindentation and nanoscratch etc., among which, the latter two can be performed by a nano indenter. Xiao and Li et al. (Li et al., 2012; Xiao et al., 2013) conducted a large number of nanoindentation tests and identified the width of old and new ITZs in RAC. In their studies, the indentation modulus of the new ITZ is close to the paste matrix, that is, the 'wall effect' is not obvious in new ITZs (Li et al., 2012; Xiao et al., 2013). The application of nanoscratch in the study of ITZs between RCA-, RGS-cement paste has been only reported in the research of geopolymer concrete (Li et al., 2021; Wei et al., 2021). Compared with grid nanoindentation, nanoscratch can obtain a series of continuous data, so the impact of uneven aggregate surface on statistical results can be mitigated (Hoover and Ulm, 2015). However, the project area of nanoscratch is larger than that of nanoindentation. When the research target is a heterogeneous material such as cement paste, the test results may be interfered by multi-phase interactions (Li et al., 2021).

Existing studies illustrate that better microscopic properties of ITZs lead to a better mechanical properties of concrete specimens (Vargas et al., 2017). Wu et al. (2022) reported that there was a superior linear correlation between micromechanical properties of ITZs and uniaxial compressive strength of concrete specimens. In the actual situation, concrete is not in a simple uniaxial compressive state but a triaxial compressive state, especially in beam-column joints and underground structures (Wang et al., 2020; Xue et al., 2023a). In addition, if the concrete is exposed to rainwater or groundwater all year round, pore water pressure would improve to a nonnegligible value (Heukamp et al., 2001). Some researchers (Malecot et al., 2019; Vu et al., 2009, 2015)

Table 1
Physical properties of coarse and fine aggregates.

Properties	NCA	RCA	NFA	RGS
Size (mm)	5–16	5–16	0.15–4.75	0.15–4.75
Apparent density (kg/m^3)	2791.5	2736.5	2615	2530
Water absorption (wt. %)	1.375	5.91	1.44	~0
Crush index (wt. %)	17	22	–	–
Fineness modulus	–	–	2.80	2.61

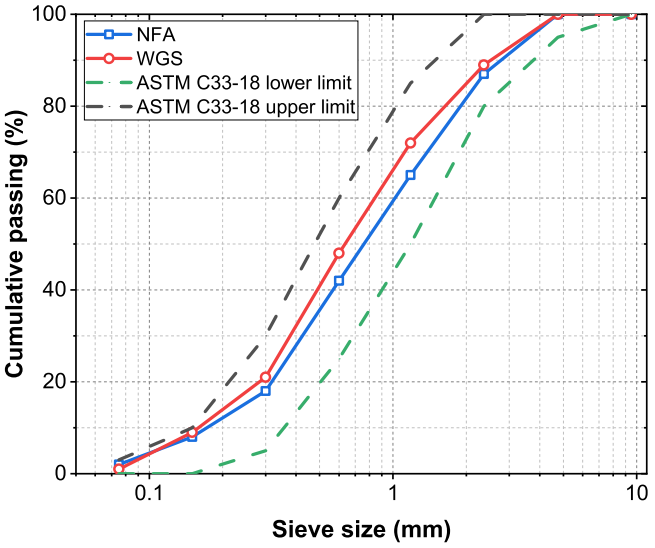

Fig. 2. Particle size distribution of fine aggregate.

tested the compressive strength of concrete with different saturation ratios under confining pressure from 50 MPa to 600 MPa and found that the compressive strength of dry concrete continued to increase with confining pressure, but the improving efficiency was limited for saturated concrete because of pore water pressure. However, the specific value of pore water pressure was not clear in their studies. Up to now, no researcher has comprehensively evaluated the microscopic properties of ITZs and macroscopic mechanical properties of sustainable concrete containing RCA and RGS under complicated stress states (Chen et al., 2024; Lei et al., 2024; Zhao et al., 2024).

In this study, 4 groups of sustainable concrete specimens were produced by adjusting the contents of RCA (50 %) and RGS (50 % and 100 %). The micromechanical properties and phases distribution of ITZs in sustainable concrete were evaluated by nanoscratch and BSE-based image analysis techniques. A triaxial multi-field coupled testing system (RTX-1000) was used to apply a confining pressure of 0–14 MPa and a pore water pressure of 0–13 MPa to Φ50 × 100 mm cylindrical concrete specimens, and the corresponding stress-strain curves were obtained. Finally, empirical models were calibrated and used to predict ultimate conditions and stress-strain curves of sustainable concrete under various stress states.

2. Experimental programme

2.1. Raw materials

The maximum particle size of 16 mm of coarse aggregate was adopted to prepare cylinder concrete specimens (Φ50 × 100 mm) (A. C33-18, 2018; G.T. 25177, 2010; G.T. 14685, 2022). Coarse aggregate of 5–10 mm and 10–16 mm each accounted for 50 % of the total. As shown in Fig. 1, natural coarse aggregate (NCA), recycled coarse aggregate (RCA), natural fine aggregate (NFA) and recycled glass sand (RGS) were selected as aggregate for concrete in this study. RCA was produced by a construction materials company from Nanchang, China, and the raw materials were a batch of waste concrete elements. The basic properties of aggregate measured according to ASTM C33-18 (A. C33-18, 2018), GB/T-25177-2010 (G.T. 25177, 2010), GB/T 14685-2022 (G.T. 14685, 2022), GB/T 14684-2022 (G.T. 14684, 2022) and GB/T-25176-2010 (G. T. 25176, 2010), and the results are listed in Table 1. As expected, the apparent density of RCA was lower than that of NCA, whereas the water absorption and crushing index were higher than that of NCA because of the old mortar attached to the surface of RCA. The apparent density of NFA was lower than that of NCA and its water absorption ratio was close to that of NCA. The water absorption of RGS can be ignored, and the apparent density was the lowest among the four aggregate, which was 2530 kg/m^3. The particle size distribution curves of NFA and RGS are shown in Fig. 2. General purpose Portland cement produced in China was mixed with tap water as matrix for concrete. Yellow-brown powdered naphthalene-base superplasticizer is used to improve the flowability of fresh concrete mixture.

2.2. Mixture design and specimen preparation

RCA had an obviously higher water absorption ratio, therefore, NCA and RCA were soaked in water for one day and allowed to a saturated surface dry (SSD) state before preparing concrete. The detailed mixture proportion of concrete specimens in this study is shown in Table 2. The numbers following RA and RG represent the replacement ratio of RCA and RGS respectively. The coarse and fine aggregate was poured into a drum mixer and mixed for 1 min, followed by cement and mixed together for another 1 min. With the mixer running continuously, tap water mixed with superplasticizer was slowly added and then continued to operate for 2 min until the ingredients were even distributed. The slump value of each group of concrete mixtures was tested as soon as the mixer stopped, and the test results are listed in the last column of Table 2. The slumps of NAC and RA50RG0 were similar because NCA and RCA were in an SSD state before mixing. However, the flowability of concrete mixture containing RGS reduced obviously, because the sharp and angular surface of RGS provided interlock force between clinkers (Ismail and AL-Hashmi, 2009). Fresh concrete mixture was added into Φ50 × 100 mm cylindrical moulds and vibrated until no large bubbles emerged. After curing in the mould for one day, the specimens were transferred to a 20 ± 2 °C and 95 % relative humidity environment for one year. The upper and lower surfaces of concrete specimens were smoothed to an error lower than 0.1 mm. The holes on the surface of specimens were sealed by cement paste with the same water-cement ratio to avoid rupture of the heat shrinkage tubing in the subsequent

Table 2
Mixture proportion of NAC and RAC specimens.

Mixes	Raw materials (kg/m^3)							Slump (mm)
	NCA	RCA	NFA	RGS	Cement	Water	SP	
NAC	1055	0	675	0	498	174	4.23	120
RA50	527.5	527.5	675	0	498	174	4.23	126
RA50RG50	527.5	527.5	337.5	337.5	498	174	4.23	105
RA50RG100	527.5	527.5	0	675	498	174	4.23	70

Note: Coarse aggregate and fine aggregate were weighted at dry state.

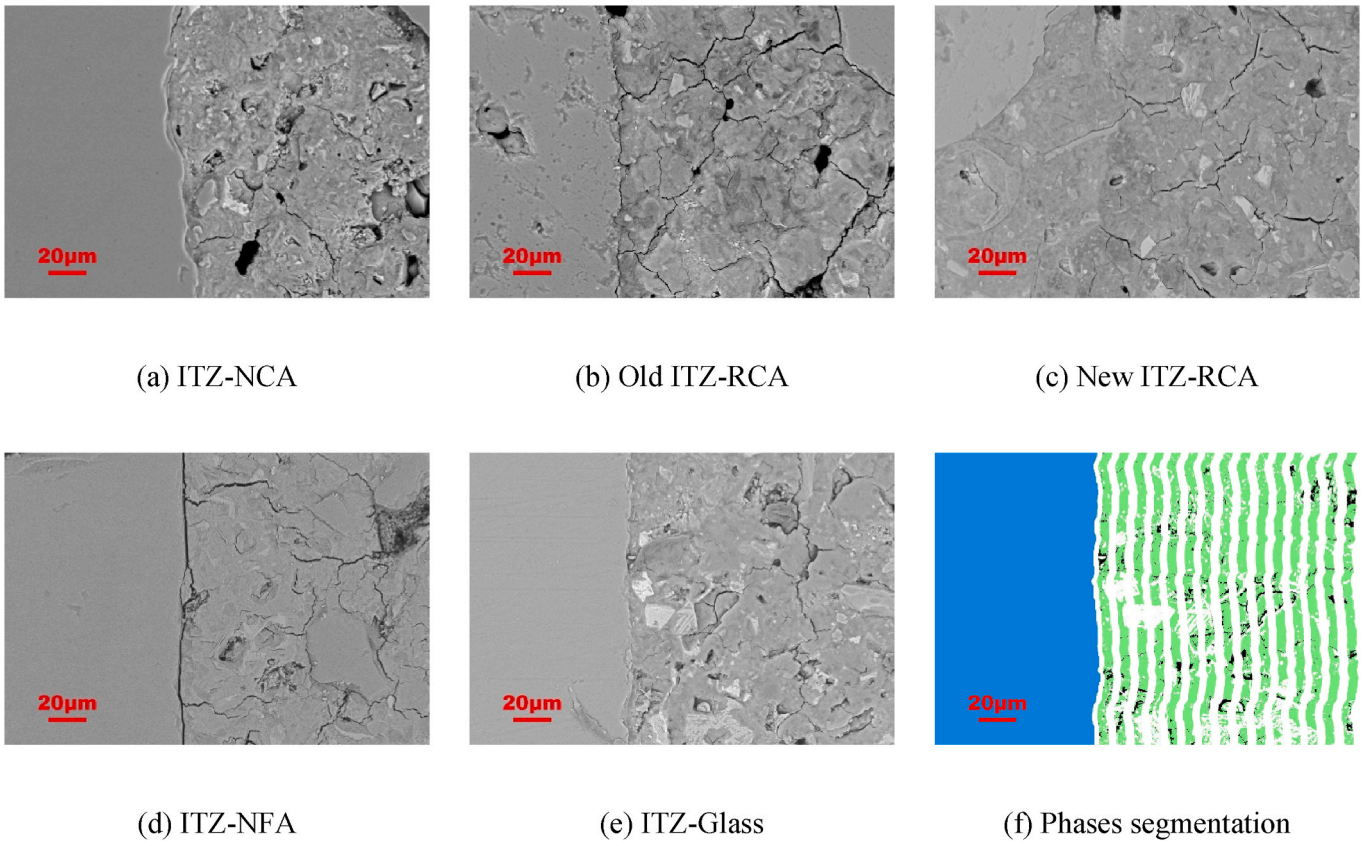

Fig. 3. Different ITZs and image analysis.

triaxial compression tests. The detailed steps of triaxial compression tests will be introduced in Section 2.4.

2.3. ITZs microscopic property tests

2.3.1. Sample preparation

A thin concrete slice containing ITZs was cut out from the middle of the cylinder concrete specimen and subsequently was impregnated by epoxy resin. After the epoxy resin solidified, 120, 240, 600 and 1200 grit abrasive paper was used to grind the sample surface. Each grit of abrasive paper was ground for 10 min 0.30 μm and 0.05 μm aluminium were used to polish the sample surface and each particle size of aluminium was polished for 30 min. To eliminate the interference of residual aluminium particles in pores and cracks on subsequent BSE-based image analysis and nanoscratch tests, the sample was placed in an ultrasonic bath for 2 min of cleaning. Finally, samples were dried in a vacuum oven at 60 °C for 48 h.

2.3.2. BSE-based image analysis

The polished surface of the sample impregnated with epoxy resin was coated with a layer of 6 nm gold. A scanning electron microscope (SEM, Zeiss EVO LS15) was used to acquire BSE images. For each ITZ, 30 BSE images with a magnification of 500 times were extracted. The contrast and brightness of each ITZ were kept consistent to facilitate image analysis.

Typical BSE images of ITZs and image analysis are shown in Fig. 3. Fifteen of 5 μm-width strips were segmented from the aggregate or old mortar boundaries to paste matrix. Since the width of ITZ in concrete is approximately between 15 and 50 μm (Scrivener et al., 2004; Rangaraju et al., 2010; Diamond and Huang, 2001), it can be reasonably inferred that the divided cement paste area contained the entire ITZ and part of paste matrix. According to the grey threshold determination method proposed by Wong et al. (Wong and Buenfeld, 2006, 2009; Wong et al., 2006), the constituents in the cement paste can be divided into hydration products, unhydrated clinkers, pores and cracks, which are represented by three colours (green represents hydration products; white represents unhydrated clinkers; black represents pores and cracks), respectively in Fig. 3 (f). From statistical analysis of the areas of different coloured regions, the variation law of constituent proportions with the distance from the aggregate boundary can be obtained.

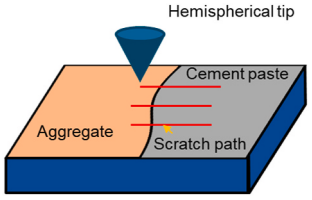

Fig. 4. Schemes of nanoscratch test for ITZs.

2.3.3. Nanoscratch tests

Nanoscratch tests were performed by an Agilent G200 Nano Indenter installed with a hemispherical tip, as shown in Fig. 4. The tip is controlled by normal force and lateral force. Based on ASTM G171-03 (A. G-171, 2017) and previous experience (Li et al., 2021; Luo et al., 2022), twice repetitive unidirectional nanoscratch with a constant normal load of 4 mN testing mode was chosen. The scratch started from the aggregate perpendicular to the interface and ended at the paste matrix. The length of each scratch path was 150 μm, of which the aggregate part was 50 μm and the cement paste part was 100 μm. The minimum spacing between scratches was 20 μm to avoid interference from overlap on test data. Nanoscratch hardness can be calculated by Eqs. (1)–(3) and used to identify ITZ width and phases.

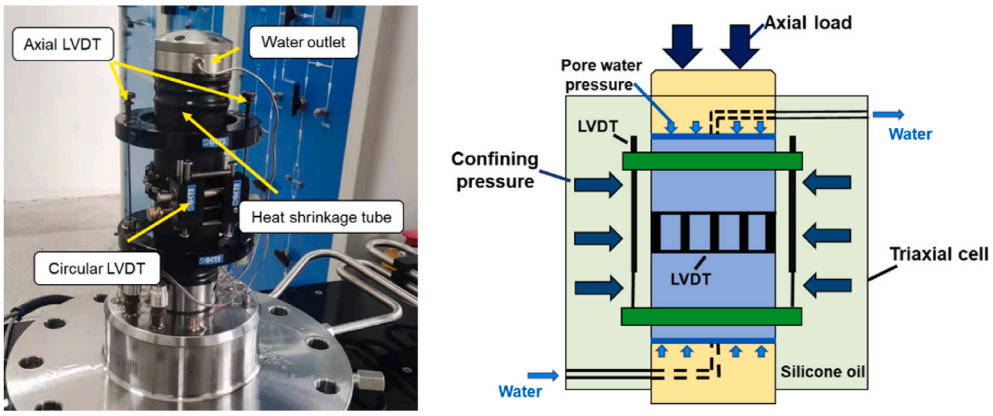

(a) Concrete specimen awaiting test (b) Scheme of multiple loads

Fig. 5. Concrete specimen multi-field coupling stress-strain curves experimental setup.

$$HS_p = \frac{8F_{Nmax}}{\pi w^2} \tag{1}$$

$$w = \begin{cases} 2\sqrt{r^2 - (r-d)^2} & d \le d_{gt} \\ w_{gt} + 2\tan\left(\frac{\alpha}{2}\right) \times (d - d_{gt}) & d > d_{gt} \end{cases} \tag{2}$$

$$d_{gt} = r\left(1 - \sin\left(\frac{\alpha}{2}\right)\right) \tag{3}$$

where HS_p is nanoscratch hardness. F_{Nmax} is the maximum normal force, which is set by 4 mN in this study. The parameter r means radius of the hemispherical tip and the value is 5 μm. Another parameter d represents nanoscratch depth. Prescratch scan and postscratch scan with a low load were conducted before and after the formal scratch to acquire surface topography along the scratch path. The scratch depth (d) can be calculated by prescratch depth subtracting from the formal scratch depth. w_{gt} and d_{gt} denote geometric transition depth and corresponding scratch width, which are 2500 nm and 5 μm, respectively. α means the apex angle of the hemispherical tip, which is 60°.

Twenty scratches were conducted for each type of ITZ and a datum was acquired for every millimetre of scratch. To avoid error when the tip was pressed into and pulled out from the sample, the data from the middle 80 μm scratch path (20 μm for aggregate and 60 μm for cement paste) were used for statistical analysis.

2.4. Triaxial compression with pore water pressure tests

2.4.1. Apparatus description

RTX-1000 multi-field coupling testing apparatus was used to apply confining pressure, pore water pressure and obtain stress-strain curves of concrete specimens under compression. The load of the system was provided by servo hydraulic pressure, which can apply a maximum confining pressure and pore water pressure of 70 MPa. The concrete specimen for triaxial compression with pore water pressure is shown in Fig. 5. During the test, the concrete specimens were put in a high-pressure triaxial chamber, where silicone oil was injected into to provide confining pressure. Pure water was injected into the sub-surface of the concrete specimen from the channel in the lower loading cap and discharged from the top surface of the specimen along the channel in the upper loading cap to provide pore water pressure. During the compression, the confining pressure and pore water pressure remained constant. The concrete specimen was covered by a heat shrinkage tube to prevent silicone oil from entering the specimen. An axial LVDT was installed on each side of the concrete specimen, and a circumferential LVDT was installed on the middle to obtain the axial and circumferential strains during the compression process.

Table 3
Loading parameters of triaxial compression with pore water pressure.

Specimens	σ_c	σ_p	Specimen	σ_c	σ_p
NAC-0	0	0	RA50RG50-0	0	0
NAC-3	3	0	RA50RG50-14	14	0
NAC-7	7	0	RA50RG50-14-5	14	5
NAC-14	14	0	RA50RG50-14-13	14	13
NAC-14-5	14	5	RA50RG100-0	0	0
NAC-14-9	14	9	RA50RG100-3	3	0
NAC-14-13	14	13	RA50RG100-7	7	0
RA50-0	0	0	RA50RG100-14	14	0
RA50-7	7	0	RA50RG100-14-5	14	5
RA50-14	14	0	RA50RG100-14-9	14	9
RA50-14-5	14	5	RA50RG100-14-13	14	13
RA50-14-13	14	13			

Note: σ_c and σ_p represents confining pressure and pore water pressure respectively.

2.4.2. Loading procedure

Four groups of concrete specimens in Table 2 were tested for their stress-strain behaviours under different stress states. Confining pressure of 0–14 MPa and pore water pressure of 0–13 MPa were applied to the concrete specimens, and the detailed loading parameters are listed in Table 3. Tests were repeat twice for each condition. The loading path was designed based on previous studies (Li et al., 2024; Tang et al., 2019, 2020b) and illustrated in Fig. 6. For uniaxial compression, a preload of 4 kN was applied to fix the specimen before the formal loading. The upper loading cap was then controlled by a strain of 0.02 %/min until the circumferential strain of the specimen reached 2–3 %. For triaxial compression, a preload of 4 kN was applied as the former loading path. Subsequently, the confining pressure and axial pressure increased simultaneously at a rate of 0.2 MPa/s to the designed value of the confining pressure, so that the specimen was at hydrostatic pressure state. Finally, the axial load was improved with an axial strain of 0.02 %/min until the circumferential strain reached 2–3 %. For triaxial compression tests with pore water pressure, the concrete specimen was vacuum-saturated in advance to ensure uniform pore water pressure. The following two steps were the same as normal triaxial compression. Pore water pressure was applied at 0.2 MPa/s to concrete specimens under hydrostatic pressure state, and maintained it for 4 h after reaching the target value. Finally, the axial load was improved at 0.02 %/min until the circumferential strain reached 2–3 % and the stress-strain curve was obtained.

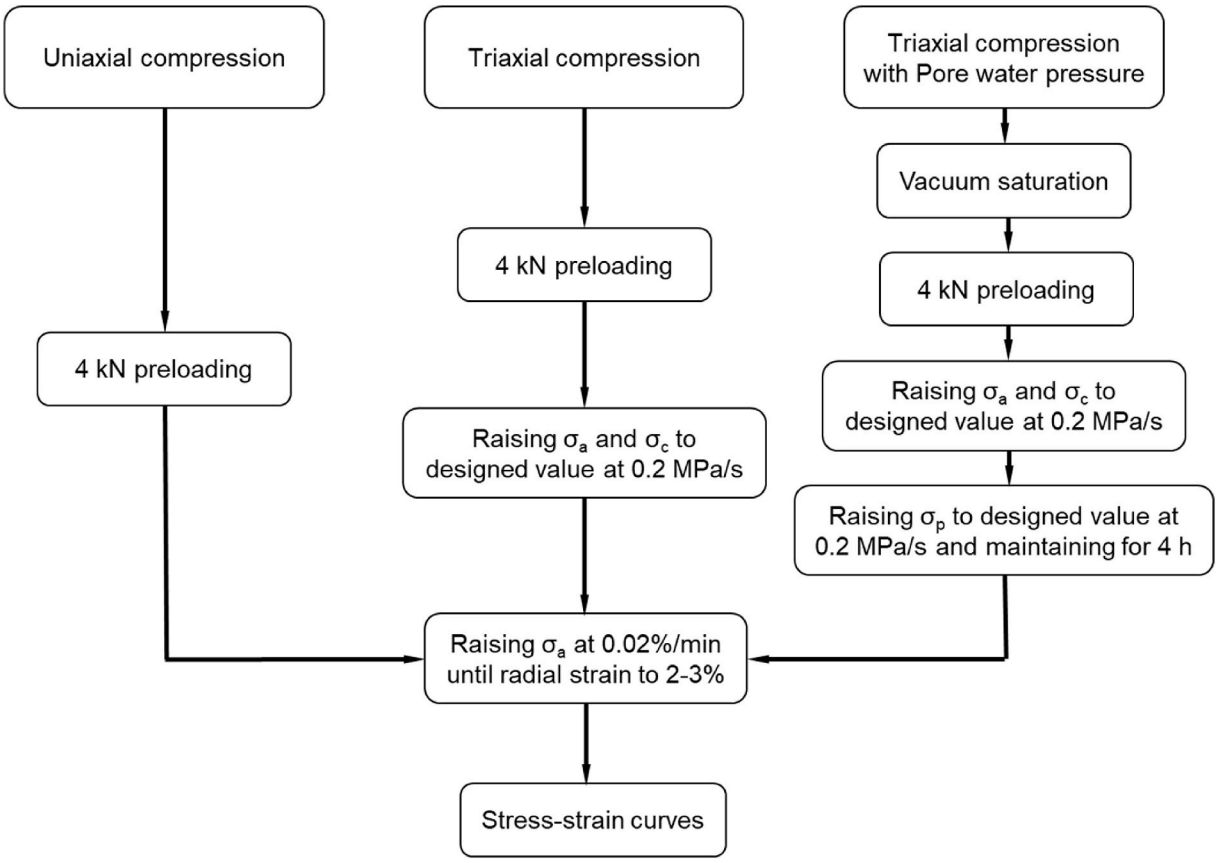

Fig. 6. Loading path of compression tests.

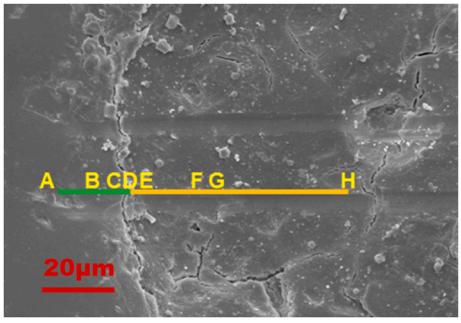

Fig. 7. Residual path after nanoscratch.

3. Results and discussions

3.1. Nanoscratch results analysis

3.1.1. ITZ thickness identification

Fig. 7 shows the microstructure of nanoscratch paths. It can be seen that the scratching paths did not overlap, indicating that the minimum spacing of 20 μm is reasonable. Cement paste has a softer texture than natural aggregate, as a result, the scratch paths were more visible on cement paste. As explained in Section 2.3.3, the middle scratch path (80 μm) were highlighted and divided by letters A-H based on nanoscratch data. Fig. 8 (a) shows the scratch hardness distribution from NCA to paste matrix and the ITZ identification procedure. The hardness of NCA was approximately 17.5 GPa, and it decreased gradually when the measurement approached the boundary. Xiao and Li et al. (Li et al., 2012; Xiao et al., 2013) also found a similar phenomenon in the nanoindentation hardness tests of RAC. This is because the strength of cement paste was much lower than that of NCA and cannot provide sufficient support for the edge of NCA, leading to a lower measured hardness at this region than the normal value (Luo et al., 2021). Due to the 'wall effect' of NCA, there were more pores and fewer unreacted clinkers within the cement paste close to the aggregate boundary (Hosan et al., 2021). Therefore, the scratch hardness was lower than the paste matrix. As the distance from the aggregate boundary increased, the scratch hardness of the paste matrix stabilised at around 1 GPa. Based on this, the test area was divided into three parts (NCA, Paste I and Paste II) based on scratch hardness distribution. Letters A-H, which are also shown in Fig. 7 were used to mark the boundaries of each part, as shown in Fig. 8 (a).

The simplified scratch hardness distribution is shown in Fig. 8 (b). The yellow and brown horizontal solid lines represent the average hardness of aggregate and Paste II respectively, where the yellow solid line was obtained from the hardness value between points A and B. Point D was the actual boundary of NCA, and the hardness of point D was much lower than the normal hardness of NCA. Therefore, point D was moved up to the average line. Point I was located at the middle of E and F, and its hardness value was an average of the test results between E and F. Symmetric targets of A, D, G, H and the two average value lines were drawn with I as the centre point. Two 'S' shape curves can be constructed for fitting key points. The tangent line was then drawn along the waist of the 'S' curve, passing through point I and intersecting the average value lines. The horizontal distances of the intersection points were W_1 and W_2 respectively. ITZ width can be calculated by the following Eq (4) (Wei et al., 2021):

$$W_{ITZ} = \frac{1}{2}W_1 + \frac{1}{2}W_2 \tag{4}$$

The calculated results are shown in Fig. 8 (d). In the previous, some researchers quantified the ITZ width by nanoindentation or image analysis techniques (Sidorova et al., 2014; Lyu et al., 2019b). However, the spacing

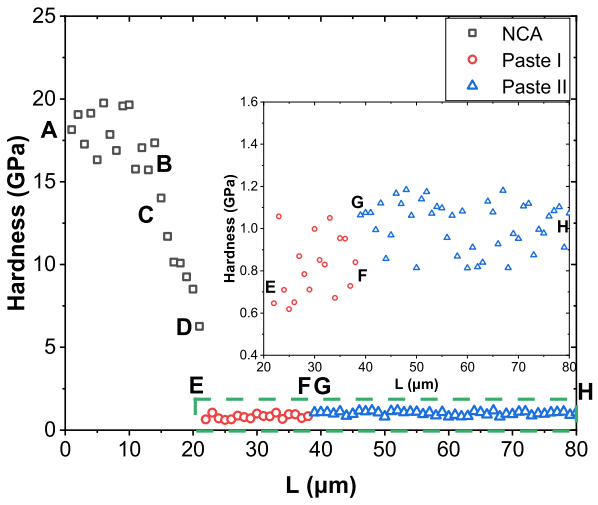

(a) Scratch hardness distribution

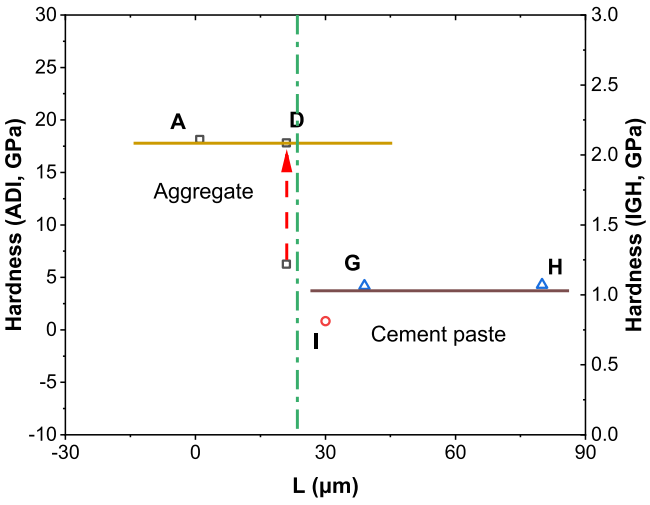

(b) Simplification of key scratch hardness

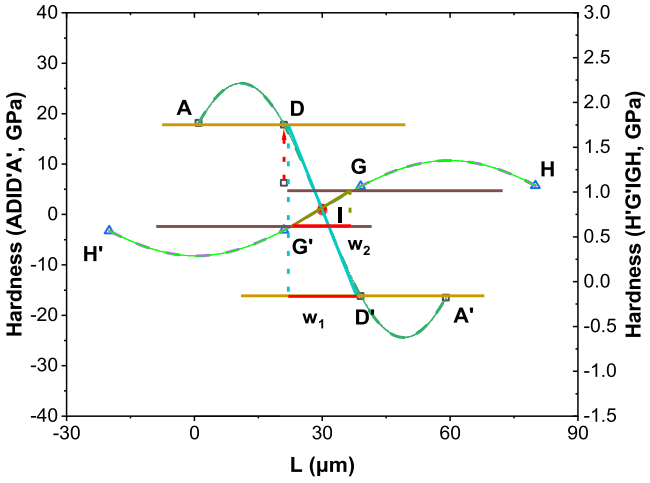

(c) Illustration of ITZ width identification

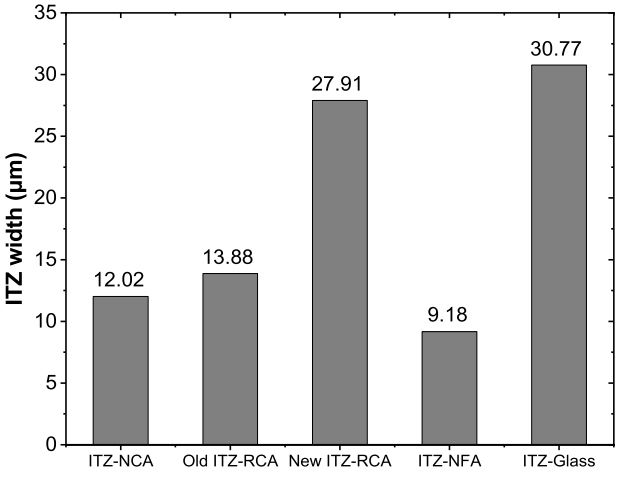

(d) Comparison of different ITZ width

Fig. 8. ITZ width identification process and results by scratch hardness.

between indentation points and the width of the strips used for image analysis were generally above 5 μm (Sidorova et al., 2014; Lyu et al., 2019b). This resulted in a minimum accuracy of 2.5 μm for the ITZ with quantification by the above two methods. In comparison, nanoscratch can obtain continuous micromechanical properties, and the calculated ITZ width had better accuracy (Wei et al., 2021). As shown in Fig. 8 (d), there were still obvious differences in the width of ITZ-NCA, New ITZ-RCA, ITZ-NFA and ITZ-Glass even with the same mixture ratio due to chemical activity and specific surface area of aggregate (Bosque et al., 2017). ITZ-NCA and Old ITZ-RCA had similar widths, about 13 μm. New ITZ-RCA and ITZ-Glass had the largest width, reaching 27.91 μm and 30.77 μm respectively. ITZ-NFA had the smallest width, only 9.18 μm. The detailed microscopic properties of ITZs are discussed in the following sections.

3.1.2. *Nanoscratch hardness frequency density analysis*

The Gaussian mixture model can be used to fit the frequency distribution histogram of scratch hardness in ITZs and analyse the contribution of phases to the micromechanical properties of ITZs. Some researchers pointed out that the scratch depth and hemispherical tip size caused the scratch hardness to hardly reflect a single phase but a combination of multiple phases (Li et al., 2021). Here, we can still infer the hydration degree and phase content within ITZs based on the minimum number of peaks (k) required for deconvolution and the frequency density of peaks. A narrow bin size for the frequency density histogram can reduce the interference caused by phase overlap within ITZs. However, a very narrow bin size would cause the shape of the histogram disordered due to insufficient data. After trial and error, the bin size was finally determined to be 0.1 GPa.

The minimum component numbers required for peak fitting of the scratch hardness frequency density distribution histogram of ITZ-NCA, Old ITZ-RCA and New ITZ-RCA were 7, 3 and 7 respectively (k = 7, 3 and 7 respectively), as shown in Fig. 9. These separated components included three main peaks (indicated by green, blue and cyan respectively), and other sub-peaks with lower proportions. The scratch hardness corresponding to the sub-peaks was higher, generally above 1.0 GPa, which is a result of mixed phase of calcium silicate hydrate (C–S–H) gel and calcium hydroxide (CH) or unhydrated clinkers (Hoover and Ulm, 2015). It can be seen that the sub-peaks containing CH and unhydrated clinkers were almost absent in Old ITZ-RCA because the old mortar attached to the RCA surface had the longest curing age and higher hydration degree. For the three main peaks (k_1, k_2 and k_3), k_1 corresponds to the smallest scratch hardness, which is mainly affected by pores and cracks; k_2 mainly represents low-density C–S–H and high-density C–S–H; k_3 mainly represents high-density C–S–H and partial CH. Pores and cracks

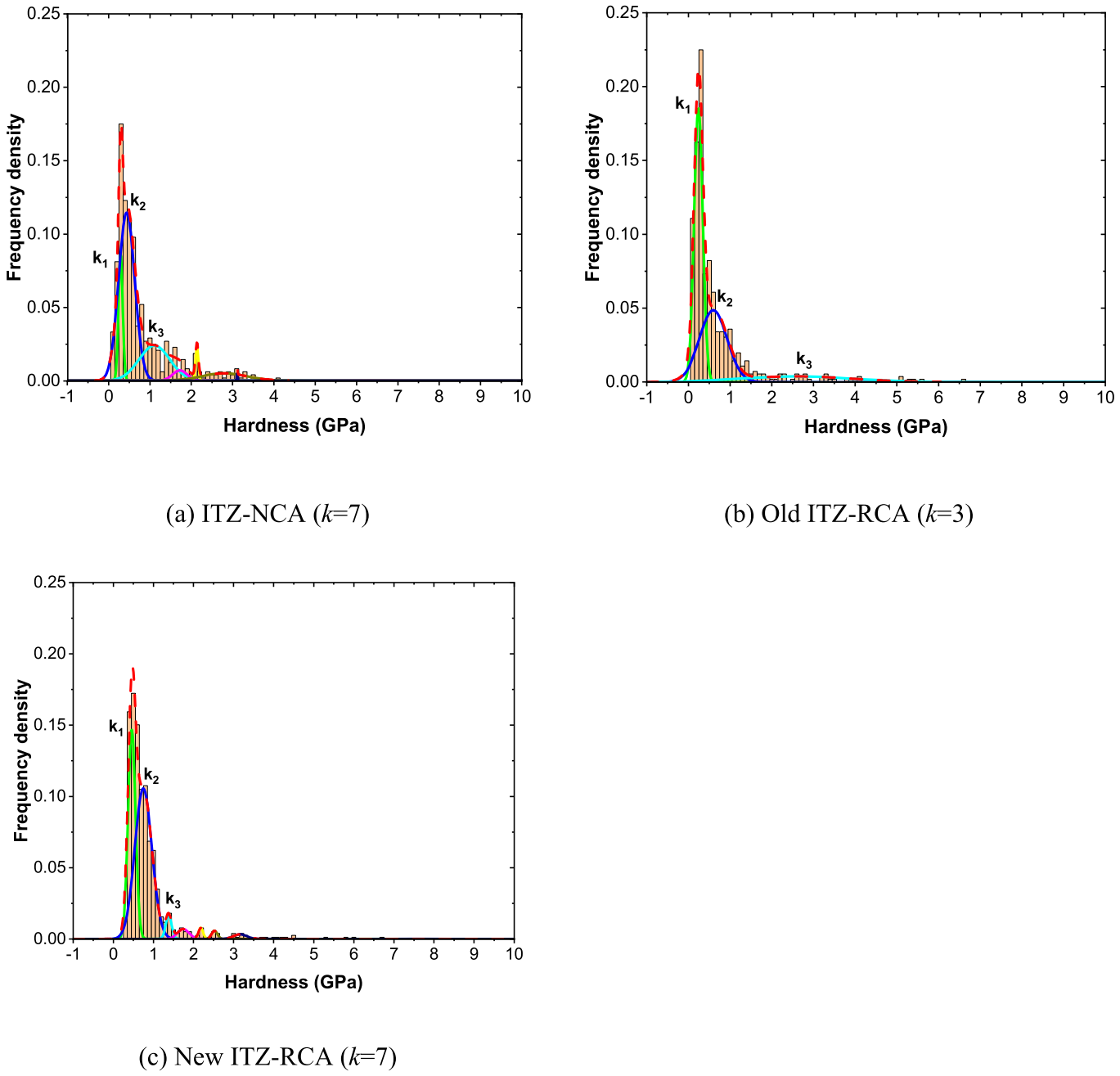

Fig. 9. Scratch hardness frequency density distribution histogram of ITZs bonded to coarse aggregate.

do not create bond strength with C–S–H. It is worth noting that the bonding between CH and C–S–H is also relatively loose (Khedmati et al., 2019). Therefore, judging the bond strength within ITZ was mainly based on the ratio of k_2. In Fig. 9, the k_2 of ITZ-NCA and New ITZ-RCA were similar, and the frequency density reached above 0.1. However, the proportion of k_2 in Old ITZ-RCA was lower as well as the proportion of k_1 was higher because the crushing process for waste concrete produced a large number of cracks within Old ITZ-RCA.

As shown in Fig. 10, there were not many sub-peaks in the scratch hardness frequency distribution histogram of ITZ-NFA and ITZ-Glass, because the high specific surface area of fine aggregate made ITZ less likely to accumulate unhydrated clinkers.k_3 was not even present within ITZ-Glass because RGS contained active SiO_2 and consumed CH in the pozzolanic reaction (Du and Tan, 2017). However, the proportion of k_1 of ITZ-Glass was prominent and even exceeded that of Old ITZ-RCA, indicating that there were many pores and cracks in ITZ-Glass and the bonding performance was loose.

The cumulative fitting curves of ITZ scratch hardness density distribution histogram is shown in Fig. 11. For ITZ in contact with coarse aggregate (see Fig. 11 (a)), Old ITZ-RCA had the smallest scratch hardness and New ITZ-RCA had the highest scratch hardness. As explained earlier, the crushing process of waste concrete created more micro-cracks within the old ITZ. Moreover, due to long-term curing, the unhydrated clinkers in the old mortar continued to hydrate, enhancing the bonding strength of New ITZ-RCA. In addition, it can be observed a shoulder at the descending stage of ITZ-NCA, Old ITZ-RCA and New ITZ-RCA curves, which is caused by the mixed phase of C–S–H and CH. In comparison, there was not a shoulder at the descending stage of ITZ-Glass curve but a single peak (see Fig. 11 (b)), because pores and cracks occupied a large proportion within ITZ-Glass. The individual peak was caused by the mixed phase of pores and low-density C–S–H gel.

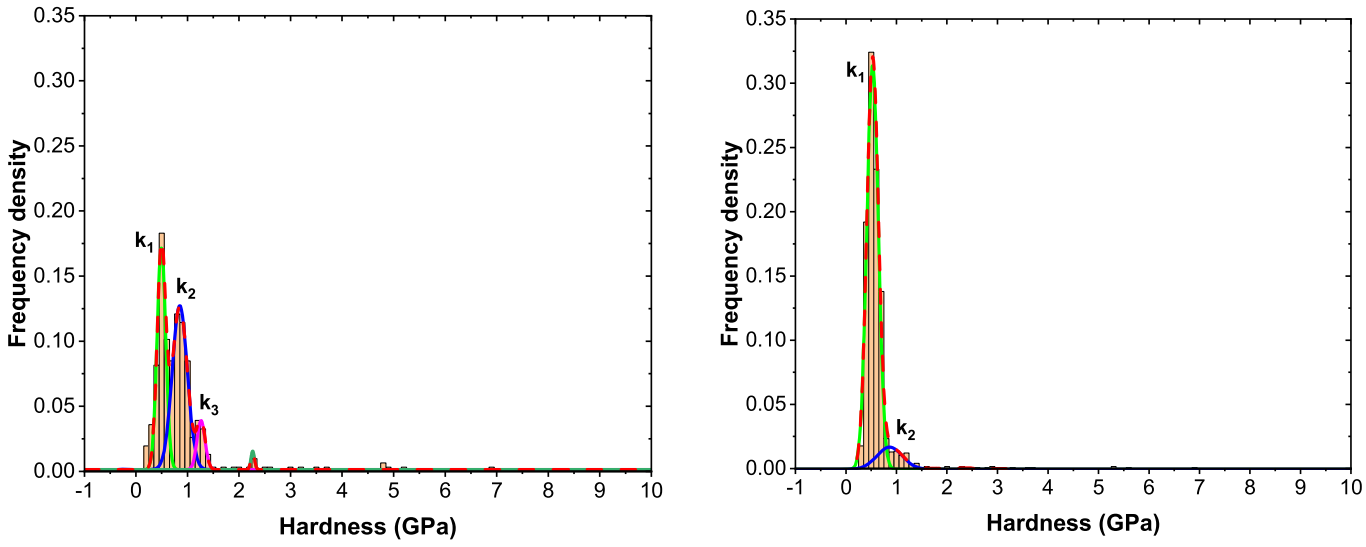

Fig. 10. Scratch hardness frequency density distribution histogram of ITZs bonded to fine aggregate.

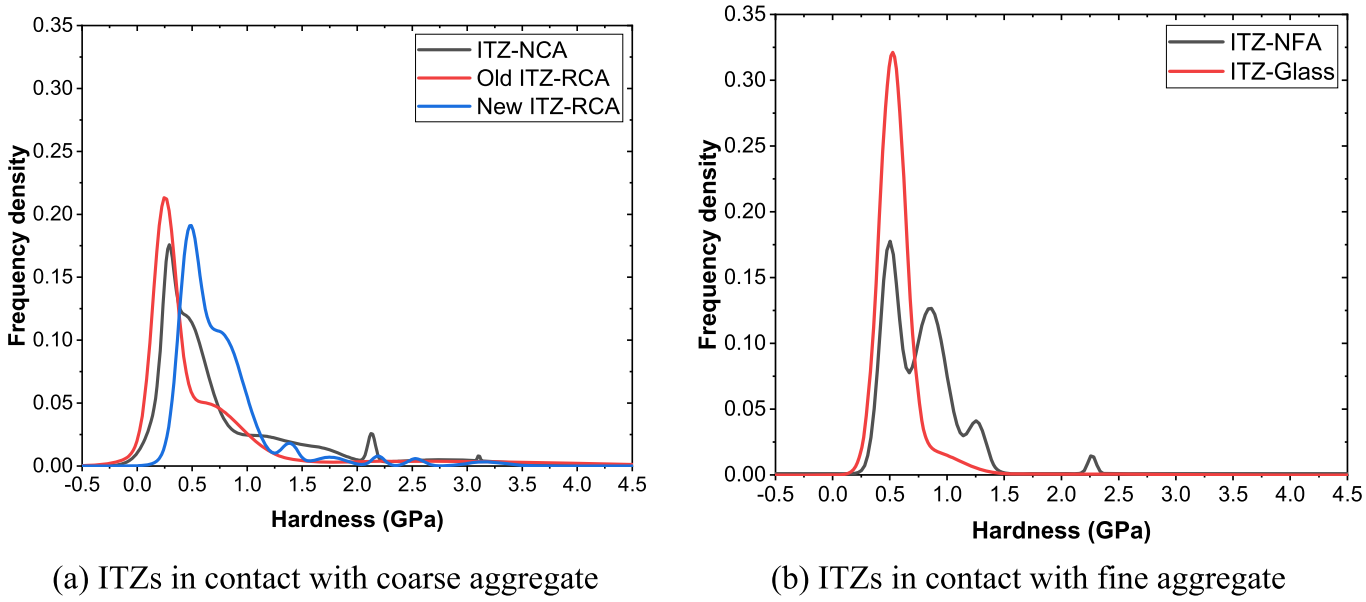

Fig. 11. Cumulative scratch hardness density distribution of ITZs.

3.2. Phase proportion and distribution from BSE-based image analysis

The statistical results for the proportion of phases within ITZs and adjacent matrix are shown in Fig. 12. Based on ITZ width identified in Section 3.1.1, the ITZ and paste matrix is divided by a dash-dot line. It can be found that the phase proportion changed most significantly within ITZs and maintained at a stable value in the paste matrix. There was a negative correlation between the content of pores and reaction products with the distance to aggregate surface. In ITZ-NCA and Old ITZ-RCA, the proportion of pores and cracks decreased rapidly between the first and second strip and was accompanied by a rapid increase in the proportion of reaction products. Meanwhile, the proportion of unreacted products gradually increased to a stable value. The porosity within ITZ-NCA was lower than that of Old ITZ-RCA and the content of unreacted products was opposite. This explained that the scratch hardness of ITZ-NCA in Section 3.1.2 was higher than that of Old ITZ-RCA. The variation of phases proportion in New ITZ-RCA was not obvious, indicating that the 'wall effect' of the old mortar was ignorable. In fact, this is reasonable. The surface of old mortar was rough and porous, prompting water permeability rather than accumulation compared to natural sand and gravel surfaces (Zhang et al., 2019). In addition, due to long-term curing, the incompletely reacted clinkers on the surface of the old mortar were further hydrated, which promoted the consistency of the phases in New ITZ-RCA. The variation law of pores, cracks and reaction products in ITZ-NFA showed a similar phenomenon to ITZ-NCA and Old ITZ-RCA, while the content of unreacted products gradually decreased instead of steadily increasing. The apparent density of NFA was close to that of NCA, as shown in Table 1, which results in easy accumulation of free water on the surface of NFA when fresh cement paste was not completely solidified. However, the specific

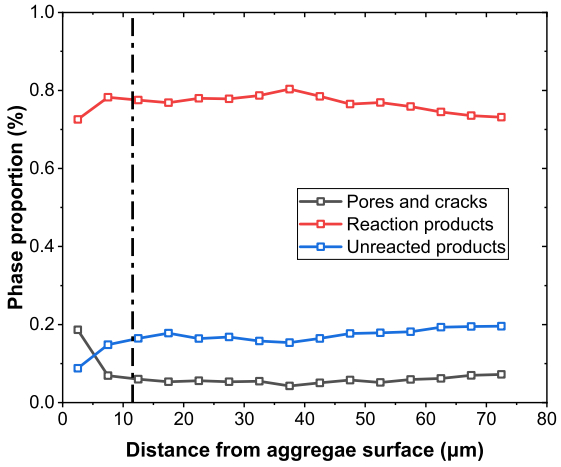

(a) ITZ-NCA

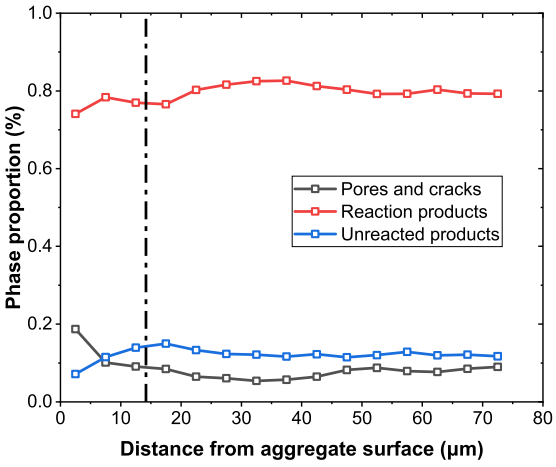

(b) Old ITZ-RCA

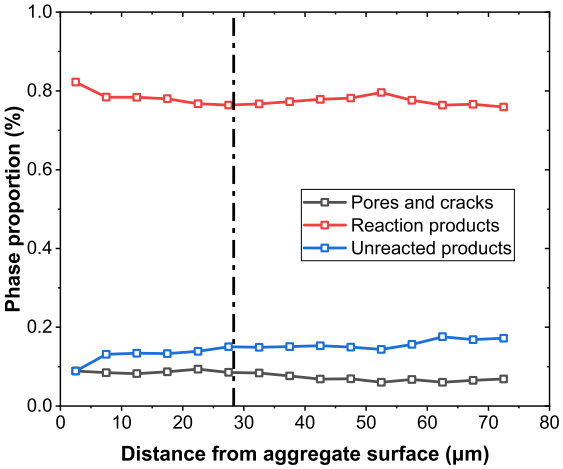

(c) New ITZ-RCA

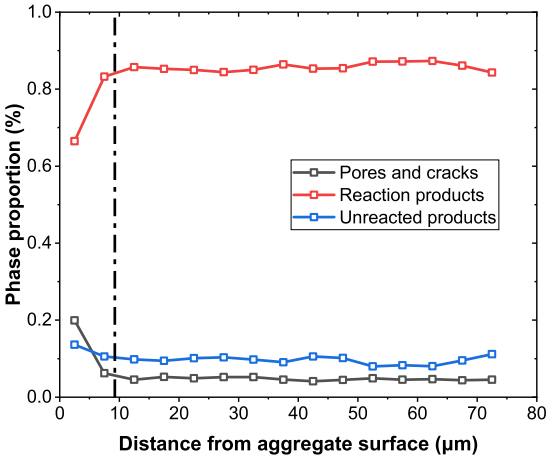

(d) ITZ-NFA

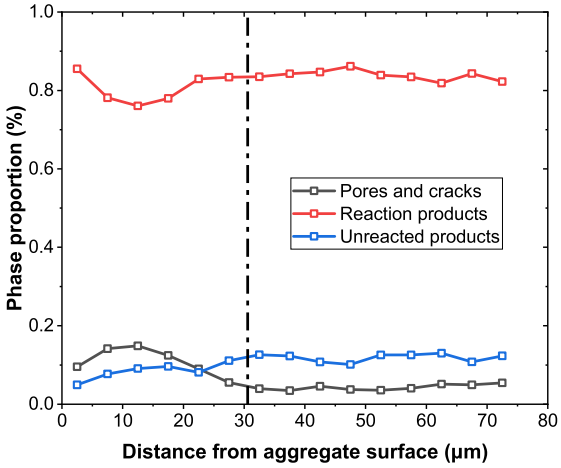

(e) ITZ-Glass

Fig. 12. Phases contents distribution within ITZs and adjacent matrix.

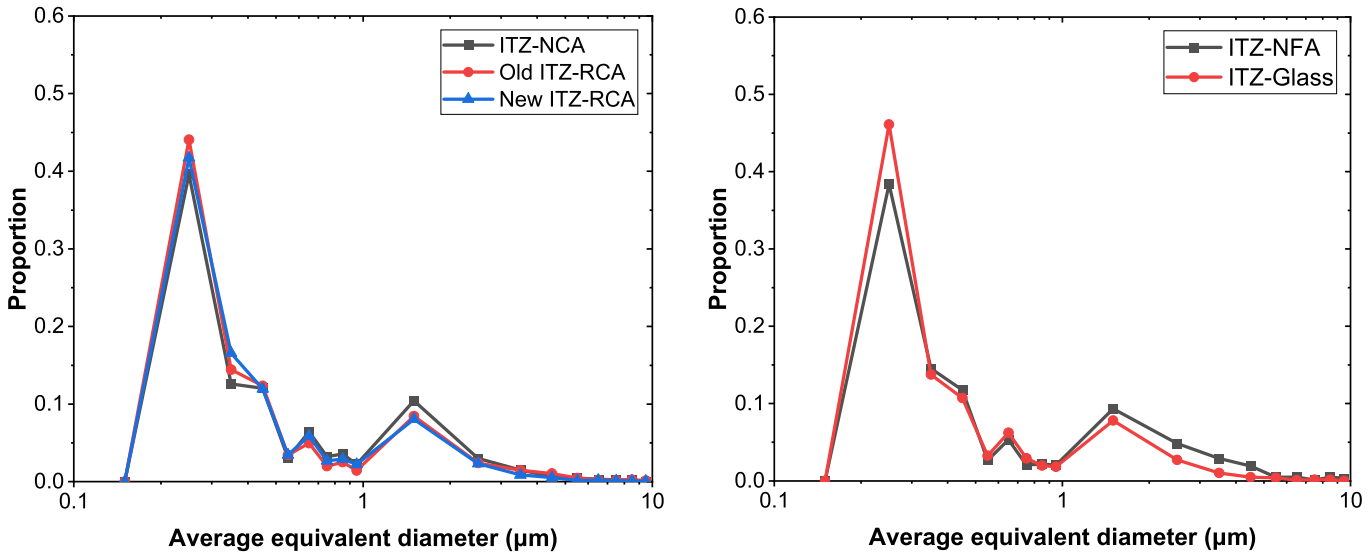

(a) ITZs in contact with coarse aggregate (b) ITZs in contact with fine aggregate

Fig. 13. Pore size distributions within ITZs.

surface area of NFA was higher and had little influence on the distribution of unreacted clinkers in ITZs. The proportion of pores and cracks in ITZ-Glass was significantly higher than the above four ITZs, which determined the worst bonding performance between RGS and cement paste. Correspondingly, the content of the reaction product dropped from 0.86 for 5 μm-strip to 0.76 for 15 μm-strip and then increased to around 0.83 in the paste matrix. Active SiO_2 in the surface of RGS participated in the pozzolanic reaction, resulting in a higher content of reaction production near the RGS surface. However, ITZ-Glass still had the highest porosity and a lower proportion of reaction products.

The pore structure of ITZs is an important feature for judging the mechanical properties and permeability of concrete. Fig. 13 shows the equivalent circle diameter of pores distribution in ITZs based on image analysis technique. It can be easily found that three peaks appeared at 0.25 μm, 0.65 μm and 1.5 μm. In general, the proportion of pores with equivalent diameters below 1 μm in ITZ-NCA was lower than that in Old ITZ-RCA and New ITZ-RCA, while the opposite was true for pores with equivalent diameters above 1 μm, especially the equivalent diameter of 1.5 μm, which accounted for 0.104 in ITZ-NCA. The proportion of pore with the equivalent diameter of 1.5 μm in Old ITZ-RCA and New ITZ-RCA was only 0.080. The difference in pore size was more pronounced for ITZs in contact with fine aggregate. ITZ-Glass had the highest proportion of pores with an equivalent diameter of 0.25 μm, reaching 0.461, whereas for ITZ-NFA was 0.384. In comparison, the proportion of pores with equivalent diameters of 1.5–4.5 μm in ITZ-Glass was lower than that in ITZ-NFA. Combined with Fig. 12, it can be concluded that ITZ-Glass had the highest porosity, and the equivalent diameter of the pores was mainly concentrated between 0.2 and 0.3 μm.

3.3. Triaxial compression with pore water pressure

3.3.1. Failure patterns

It can be seen from Fig. 14 that the failure patterns of each group of concrete specimens changed with the stress states in a similar manner. The concrete specimens experienced circumferential expansion during the compression process and generated vertical cracks when there was no confining pressure and pore water pressure. The circumferential splitting failure mode finally appeared. When the specimen was subjected to confining pressure, numerous vertical cracks transformed into a single oblique crack and exhibited a shear failure mode. Pore water pressure had little effect on the failure mode of concrete specimens. It is worth noting that a small number of vertical cracks appeared on the surface of RA50-14-13 instead of a single oblique crack. This is probably due to the cancellation of pore water pressure and confining pressure, resulting in a uniaxial compression-like failure mode for the concrete specimen.

3.3.2. Stress-strain curves analysis

The stress-strain curves of four groups of concrete specimens are shown in Fig. 15. For uniaxial compression, the axial stress-strain curves of NAC and RA50 reached the peak value almost without axial deformation and rapidly entered the descending part. On the contrary, the lateral deformation was more obvious, and the peak radial strain was −0.159 % and −0.372 % respectively. This corresponds to the uniaxial compression failure mode of NAC and RA50 in Fig. 14. When the concrete specimens contained 50 % and 100 % RGS, the peak stress decreased and the plastic deformation capacity improved. This is because the higher porosity within ITZ-Glass provided more space for axial deformation before failure.

When concrete specimens were subjected to triaxial compression, the peak stress was significantly enhanced compared to uniaxial compression, because circumferential confinement increased the internal friction angle of concrete specimens. The axial peak strain of NAC, RA50RG50 and RA50RG100 gradually increased with confining pressure and the descending part became gentle, showing a plastic failure characteristic. This is because the pores and cracks in concrete specimens closed after applying confining pressure, which limited the expansion of new cracks during compression. RA50 behaved differently in triaxial compression. Although the peak axial strain of RA50 at confining pressure of 7 MPa and 14 MPa improved compared to uniaxial compression, the RA50-14 showed some brittle characteristics in the descending part. According to the analysis in Section 3.1 and 3.2, the scratch hardness of ITZs in RA50 was higher and had a dense microstructure, making it prone to brittle failure.

Furthermore, when pore water pressure existed, the peak stress and axial peak strain of concrete specimens were reduced. The pore water provided a supporting force in pores and improved the resistance of concrete to compressive deformation at initial stage. On the other hand, pore water promoted the propagation of cracks in concrete specimens

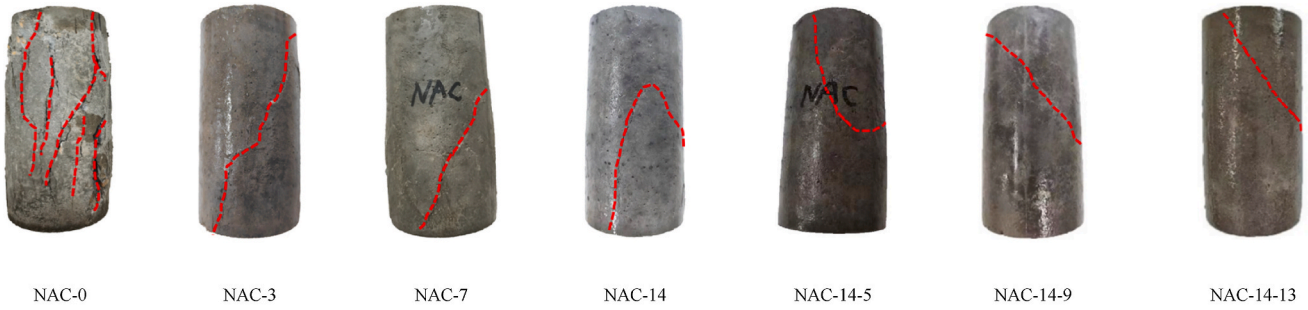

(a) NAC under different confining pressure and pore water pressure

(b) RA50 under different confining pressure and pore water pressure

(c) RA50RG50 under different confining pressure and pore water pressure

(d) RA50RG100 under different confining pressure and pore water pressure

Fig. 14. Failure patterns of RAC with RGS under triaxial compression and pore water pressure.

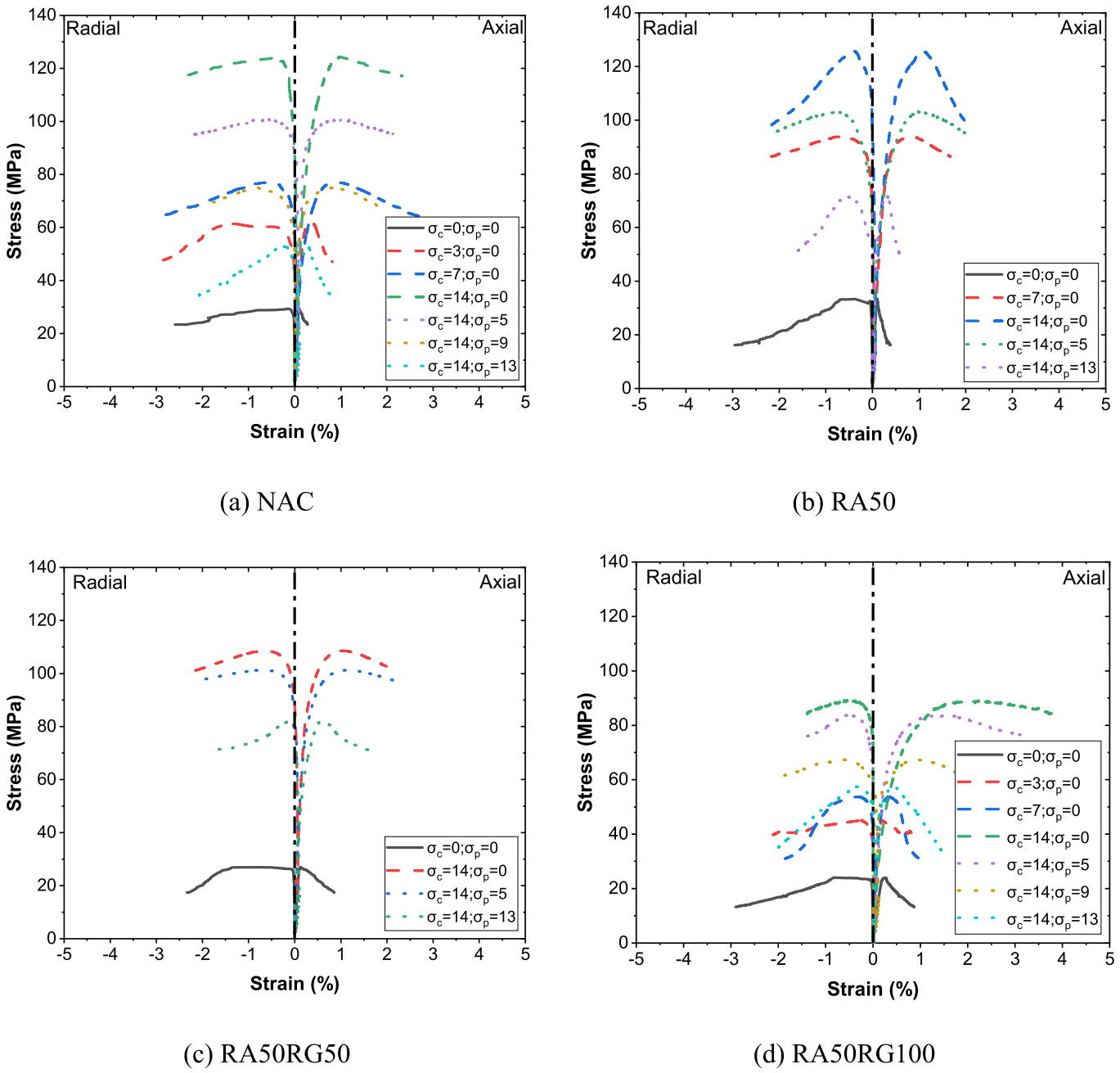

Fig. 15. Stress-strain curves of sustainable concrete specimens under confining pressure and pore water pressure.

during compression. When the pore water pressure reached 13 MPa, the four groups of concrete specimens showed obvious brittle failure characteristics.

3.3.3. *Axial stress-volumetric strain curves analysis*

The volumetric strain of concrete specimens during compression can be calculated according to the following formula:

$$\varepsilon_v = \varepsilon_a + 2 \times \varepsilon_c \tag{5}$$

where, ε_a and ε_c represents axial and circumferential strain respectively.

The axial stress-volumetric strain curves of the four groups of concrete specimens are shown in Fig. 16. The positive volumetric strain means that the specimen was in a compression state and vice versa. The maximum volumetric strain was directly related to the stress state and the pore structure of ITZs. The micromechanical properties and microstructure of ITZs in NAC and RA50 were better than the latter two groups of specimens. As a result, NAC and RA50 quickly transformed into an expansion deformation state after experiencing a brief compression process under uniaxial compression. When the NFA in concrete specimens was replaced by RGS, the compression deformation under uniaxial compression was more obvious. Especially for RA50RG100, the maximum volumetric strain under uniaxial compression increased to 0.1206 % compared to 0.0485 % of NAC.

The confining pressure limited the circumferential expansion of concrete specimens. Therefore, the compression deformation increased significantly. When the confining pressure was 14 MPa, the maximum volumetric strain of NAC, RA50, RA50RG50 and RA50RG100 reached 0.3982 %, 0.4781 %, 0.312 % and 1.1518 % respectively. Among them, Fig. 16 (d) shows that when RA50RG100 was subjected to a confining pressure of 14 MPa, the specimen was always in a compression state until failure. This is because the high porosity within ITZ-Glass provided enough space for compressive deformation. In addition, the triaxial

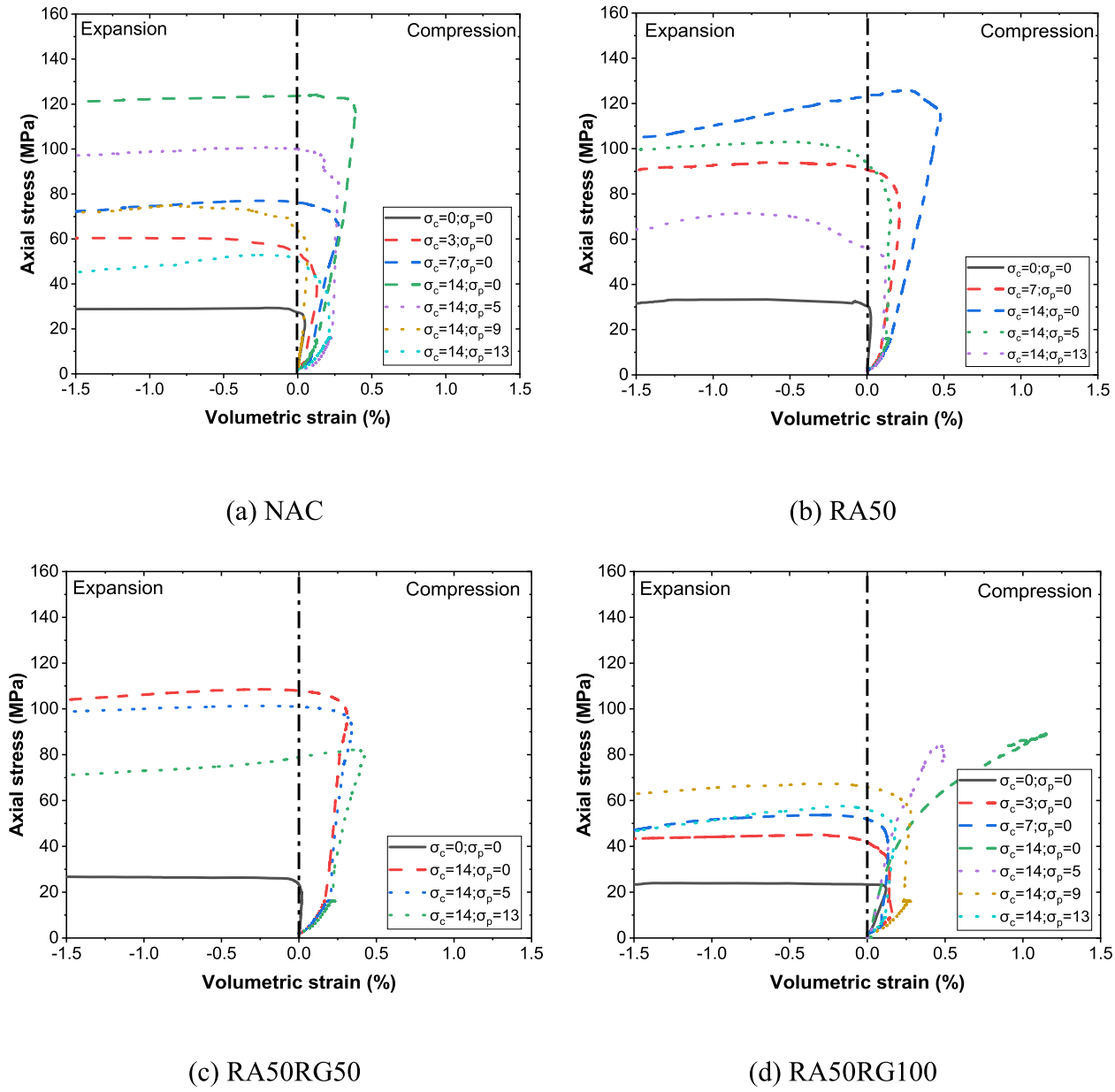

Fig. 16. Axial stress-volumetric strain curves of sustainable concrete specimens under confining pressure and pore water pressure.

compressive strength of RA50RG100 was obviously lower than the former three groups of specimens (the triaxial compressive strength of RA50RG100-14 was only 89.19 MPa), resulting in the loss of bearing capacity before expansion deformation occurred. However, it is difficult to be reflected in specimen failure patterns. Although the crack distribution was similar to other stress conditions, there were still differences in the circumferential expansion and displacement of the cylinder specimens.

When pore water pressure existed, the maximum volumetric strain of NAC and RA50 reduced under triaxial compression, mainly due to the supporting function of pore water before the crack propagation. The maximum volumetric strain of RA50RG50 gradually increased with pore water pressure, which is probably because of its low triaxial compressive strength. In the process of improving pore water pressure, more cracks were generated in concrete specimens, thereby increasing the axial deformation. When the pore water pressure was low (σ_p = 5 MPa), RA50RG100 was still in a compressed state until failure, while for the pore water pressure of 9 MPa and 13 MPa, the expansion deformation reappeared because the pore water pressure offset the influence of confining pressure.

3.3.4. *Ultimate condition*

The representative mechanical data of concrete specimens were extracted from Figs. 15 and 16 and listed in Table 4. The elastic modulus was defined as the slope of the stress-strain curve between axial strain of 0.005 % and 40 % of peak stress according to ASTM C469. To highlight the changes in the mechanical properties of concrete specimens with confining pressure and pore water pressure, the data in Table 4 were normalised and shown in Fig. 17a,b.

3.3.4.1. Peak stress and elastic modulus. It can be seen from Fig. 17(a) that the compressive strength of concrete specimens gradually increased with confining pressure. For a confining pressure ratio of 0.5, the triaxial compressive strength can be increased by more than 4 times than the uniaxial compressive strength. However, the improving efficiency on the peak stress reduced with the content of RGS. Circumferential confinement improved the microstructure of concrete and enhanced the internal friction between phases. Some studies pointed out that concrete with

Table 4
Testing results extracted from stress-strain curves.

Specimens	σ_c (MPa)	σ_p (MPa)	f_c (MPa)	S.D.	ε_{ap} (%)	ε_{cp} (%)	ε_{vm} (%)	E (GPa)	S.D.
NAC-0	0	0	29.36	1.66	0.101	−0.159	0.0485	30.35	1.36
NAC-3	3	0	61.38	1.93	0.381	−0.466	0.1285	35.71	1.24
NAC-7	7	0	76.99	2.31	0.911	−0.611	0.2794	35.51	2.21
NAC-14	14	0	124.31	1.34	0.973	−0.430	0.3982	42.10	1.07
NAC-14-5	14	5	100.79	1.68	0.924	−0.559	0.2784	53.09	3.03
NAC-14-9	14	9	74.98	3.21	0.784	−0.789	0.0642	60.54	2.15
NAC-14-13	14	13	52.9	1.12	0.273	−0.248	0.2168	67.82	1.69
RA50-0	0	0	33.35	2.58	0.099	−0.372	0.0252	40.59	2.16
RA50-7	7	0	93.81	1.62	0.899	−0.768	0.2118	30.96	3.56
RA50-14	14	0	125.87	2.06	1.070	−0.411	0.4781	38.72	2.45
RA50-14-5	14	5	103.1	1.24	0.998	−0.744	0.1551	52.93	2.36
RA50-14-13	14	13	71.5	2.33	0.312	−0.551	0.1214	65.68	1.87
RA50RG50-0	0	0	26.92	1.63	0.129	−0.661	0.0515	29.84	1.71
RA50RG50-14	14	0	108.59	5.07	1.044	−0.630	0.312	43.48	5.85
RA50RG50-14-5	14	5	101.33	5.53	1.179	−0.738	0.341	50.37	5.79
RA50RG50-14-13	14	13	82.19	5.57	0.592	−0.111	0.423	42.77	3.43
RA50RG100-0	0	0	23.97	1.49	0.280	−0.842	0.1206	12.61	3.11
RA50RG100-3	3	0	45.05	4.16	0.185	−0.234	0.2379	28.75	3.62
RA50RG100-7	7	0	53.68	2.39	0.335	−0.311	0.1342	34.51	1.14
RA50RG100-14	14	0	89.19	3.73	2.246	−0.549	1.1518	23.14	4.40
RA50RG100-14-5	14	5	83.67	5.79	1.611	−0.566	0.4973	30.26	4.74
RA50RG100-14-9	14	9	67.31	5.82	0.929	−0.628	0.2792	65.69	3.71
RA50RG100-14-13	14	13	57.61	1.79	0.418	−0.278	0.1802	38.16	4.03

Note: σ_c and σ_p represent confining pressure and pore water pressure respectively; f_c represents compressive strength of concrete specimens under various stress states; ε_{ap} and ε_{cp} represent axial peak strain and circumferential peak strain respectively; ε_{vm} represents the maximum volumetric strain; E represents elastic modulus; S.D. means standard deviations.

lower strength had a more obvious improvement ratio in triaxial compression (Chen et al., 2017; Meng et al., 2017; Deng et al., 2017). The test results in this study contradict some previous conclusions because the bonding strength between cement paste and RGS was weaker than normal ITZs (see Fig. 10). When cracks extended to RGS, they were more likely to propagate along ITZ-Glass rather than penetrating RGS directly. When pore water pressure existed, the situation was opposite. The relative peak stress of NAC and RA50 decreased faster with pore water pressure. This is probably because ITZ-NCA and ITZ-NFA contained more unhydrated clinkers, and their ability to resist the effect of pore water pressure on crack expansion was not as good as ITZ-Glass with less CH and unhydrated clinkers, especially when numerous pores were compressed by circumferential confinement. As shown in Fig. 17(b) both confining pressure and pore water pressure can increase the elastic modulus of concrete specimens. Confining pressure posed the concrete microstructure denser, whereas the supporting effect of pore water improved the initial stiffness of concrete specimens under compression.

3.3.4.2. Peak strain and maximum volumetric strain. As shown in Fig. 17 (c)–(e) relative deformation also has a close relationship with confining pressure and pore water pressure. The axial peak strain of NAC and RA50 increased rapidly with confining pressure and then slowed down. At a relative confining pressure of 0.3, the relative axial peak strain of RA50RG100 remained constant. However, as the relative confining pressure approached 0.6, the relative axial strain increased significantly. This increase is also attributed to the high porosity present in the ITZ-Glass. The supporting effect of pore water reduced the axial peak strain, which was more obvious for concrete specimens with higher micromechanical properties. Similar phenomena were also reflected in the maximum volumetric strain. The strengthening effect of confining pressure on the ductility and the supporting effect of pore water pressure caused the relative volumetric strain in Fig. 17(c) to increase at first and then decrease. In comparison, the change pattern between circumferential peak strain, confining pressure and pore water pressure was not obvious, because it was affected by many accidental factors, including the irregular expansion of specimens. The circumferential peak strain of RA50RG50 and RA50RG100 was not significantly different from that of uniaxial compression, whereas the circumferential peak strain of NAC under triaxial compression with and without pore water pressure was more than twice that of uniaxial compression. This provides further evidence that RGS increased the porosity of concrete specimens and allowed for more axial compression space.

4. Failure criteria

4.1. Failure criteria for triaxial compression

4.1.1. Mohr-Coulomb failure criterion

Mohr-Coulomb failure criterion is a classic linear theory considering normal stress and maximum shear stress. It was first proposed and applied to analyse the failure surface of clay. Nowadays, it has been widely used to describe the critical state of concrete materials under uniaxial and triaxial compression. The criterion can be described as below (Li et al., 2022; Yang et al., 2022):

$$\frac{f_c}{f_{c0}} = a_1 \frac{\sigma_c}{f_{c0}} + 1 \tag{6}$$

where, f_{c0} and f_c represent uniaxial compressive strength and triaxial compressive strength respectively; σ_c represents confining pressure; a_1 can be calculated by $\frac{1+sin\,\varphi}{1-sin\,\varphi}$ and φ means the internal friction angle of concrete (Li et al., 2022). Confining pressure improves the strength and ductility of concrete specimens by improving the internal friction and limiting cracks expansion of concrete. The strengthening efficiency of the confining pressure on concrete specimens becomes more obvious as a_1 increases. The Mohr-Coulomb equations for concrete containing RCA and RGS can be obtained by regression analysis of the data in this study:

$$\text{NAC, RA50}\ \frac{f_c}{f_{c0}} = 6.93 \frac{\sigma_c}{f_{c0}} + 1 \tag{7}$$

$$\text{RA50RG50, RA50RG100}\ \frac{f_c}{f_{c0}} = 5.13 \frac{\sigma_c}{f_{c0}} + 1 \tag{8}$$

The fitting results of Mohr-Coulomb failure criterion on the test data is shown in Fig. 18. Meanwhile, the existing experimental data (Meng et al., 2017; Chen et al., 2019; Folino and Xargay, 2014) on RAC triaxial compression are also presented in Fig. 18. The a_1 value of

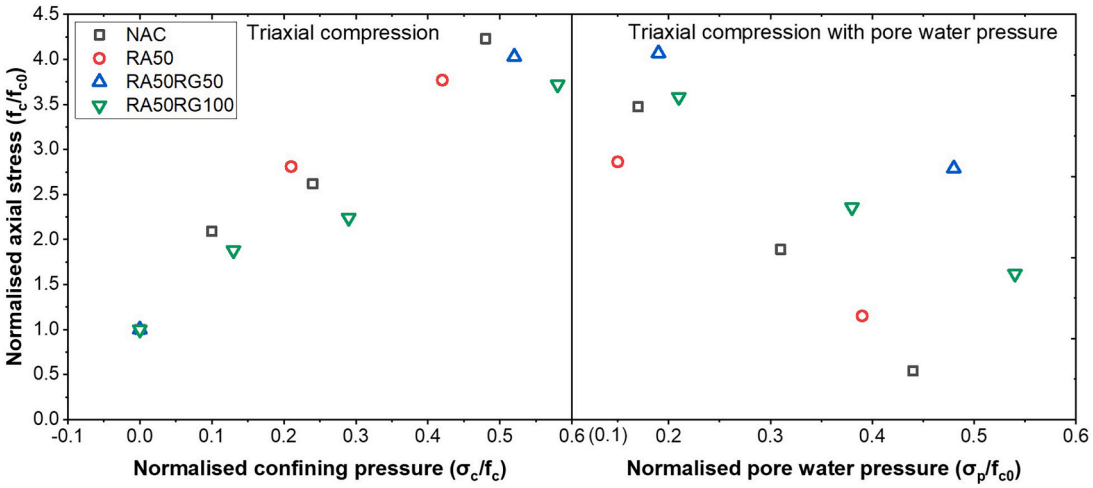

(a) Relative axial peak stress at triaxial compression with pore water pressure

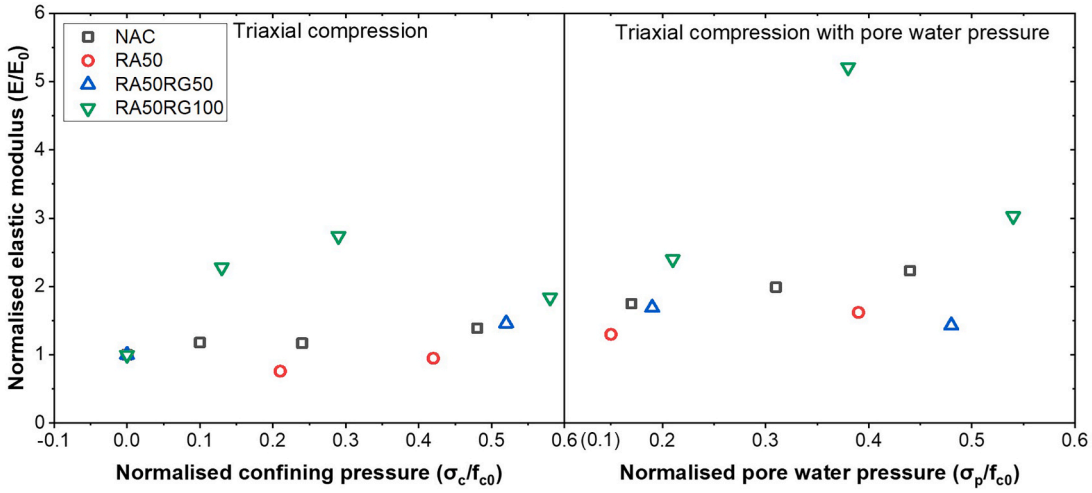

(b) Relative elastic modulus at triaxial compression with pore water pressure

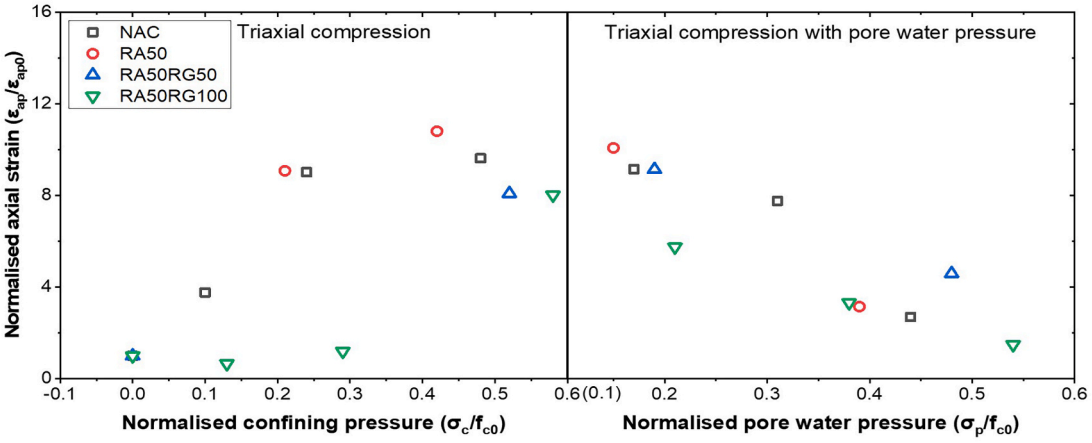

(c) Relative axial peak strain at triaxial compression with pore water pressure

Fig. 17a. Ultimate states of sustainable concrete specimens under various stress states. (a) Relative axial peak stress at triaxial compression with pore water pressure. (b) Relative elastic modulus at triaxial compression with pore water pressure. (c) Relative axial peak strain at triaxial compression with pore water pressure

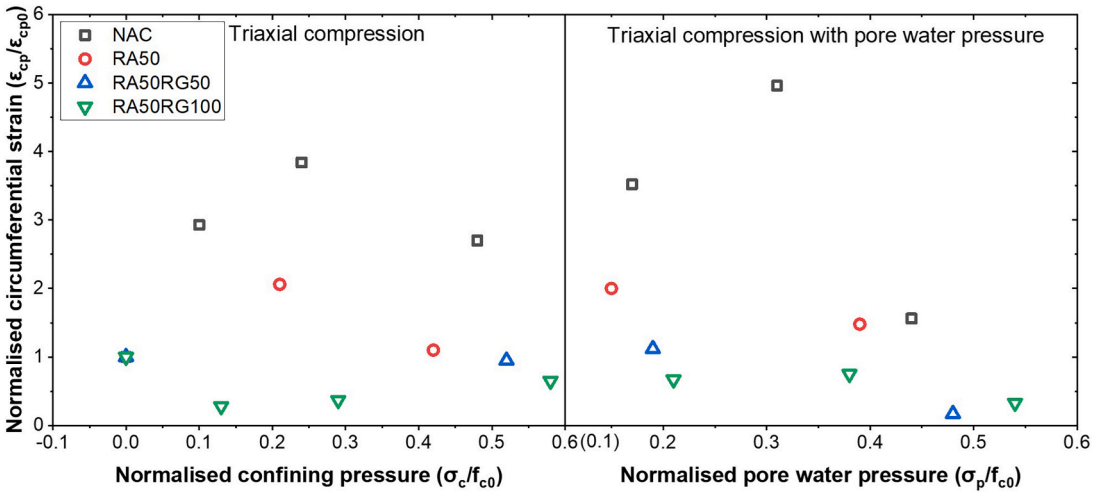

(d) Relative circumferential peak strain at triaxial compression with pore water pressure

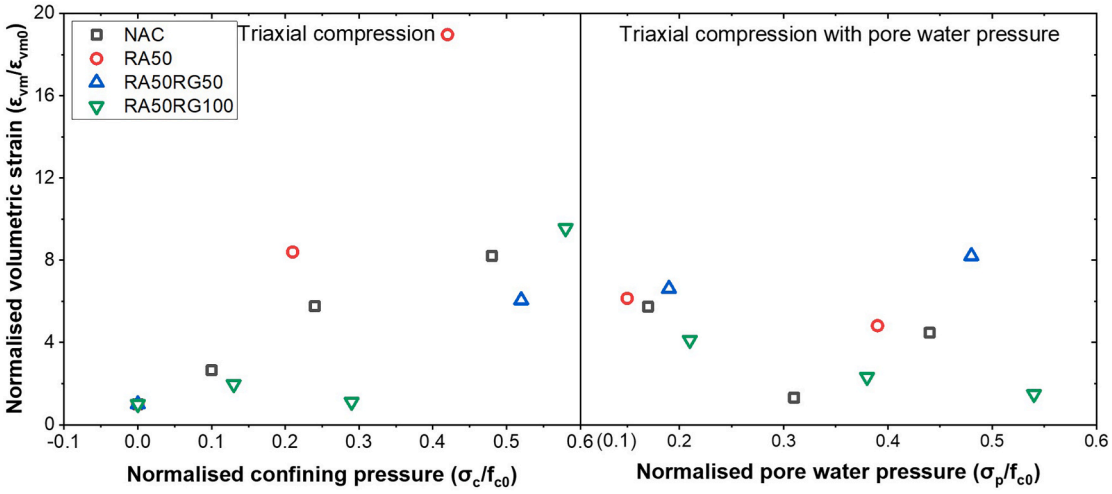

(e) Relative volumetric strain at triaxial compression with pore water pressure

Fig. 17b. Ultimate states of sustainable concrete specimens under various stress states. (d) Relative circumferential peak strain at triaxial compression with pore water pressure. (e) Relative volumetric strain at triaxial compression with pore water pressure

Mohr-Coulomb failure criterion is in a reasonable range. RCA would not change the internal friction angle of concrete, which is consistent with conclusions in other research (Chen et al., 2019). The a_1 values of RA50RG50 and RA50RG100 were lower than those of NAC and RA50 because the higher porosity in ITZ-Glass weakened the efficiency of the confining pressure in improving the internal friction of phases in concrete.

4.1.2. William-Warnke failure criterion

William-Warnke failure criterion is a five-parameter model widely used in finite element software such as failure surface analysis by ANSYS. When the confining pressure is low, it can be simplified to a three-parameter model as Eq. (9) (Wu et al., 2023).

$$\frac{\tau_m}{f_{c0}} = a_2 + b_2\left(\frac{\sigma_m}{f_{c0}}\right) - c_2\left(\frac{\sigma_m}{f_{c0}}\right)^2 \tag{9}$$

where a_2, b_2 and c_2 are parameters; σ_m and τ_m are principal axial stress and principal shear stress, which can be calculated by $\sigma_m=(\sigma_1+\sigma_2+\sigma_3)/3$ and $\tau_m = \frac{1}{\sqrt{15}}[(\sigma_1-\sigma_2)^2+(\sigma_1-\sigma_3)^2+(\sigma_2-\sigma_3)^2]^{0.5}$, respectively. σ_1, σ_2 and σ_3 are principal stress in three directions. The William-Warnke failure criterion for concrete specimens in this study are displayed in Eqs. (10) and (11).

$$\text{NAC and RA50}\ \frac{\tau_m}{f_{c0}} = 0.091 + 0.857\left(\frac{\sigma_m}{f_{c0}}\right) - 0.071\left(\frac{\sigma_m}{f_{c0}}\right)^2 \tag{10}$$

$$\text{RA50RG50 and RA50RG100}\ \frac{\tau_m}{f_{c0}} = 0.186 + 0.546\left(\frac{\sigma_m}{f_{c0}}\right) + 0.045\left(\frac{\sigma_m}{f_{c0}}\right)^2 \tag{11}$$

The fitting curves and test data in this study are shown in Fig. 19. Similarly, existing triaxial compression test data (Meng et al., 2017; Chen et al., 2019; Folino and Xargay, 2014) on RAC was also collected and presented in Fig. 19. The William-Warnke failure curves obtained based on the data in this study are within a reasonable range. A satisfying fitting result can be achieved for both concrete specimens with and without RGS.

4.1.3. Power-law failure criterion

The power-law failure criterion suggests that the peak stress of

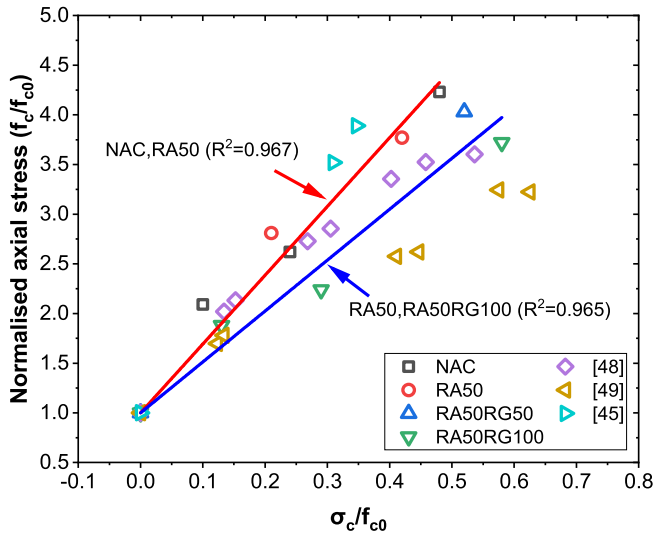

Fig. 18. Fitting performance of Mohr-Coulomb failure criterion under triaxial compression.

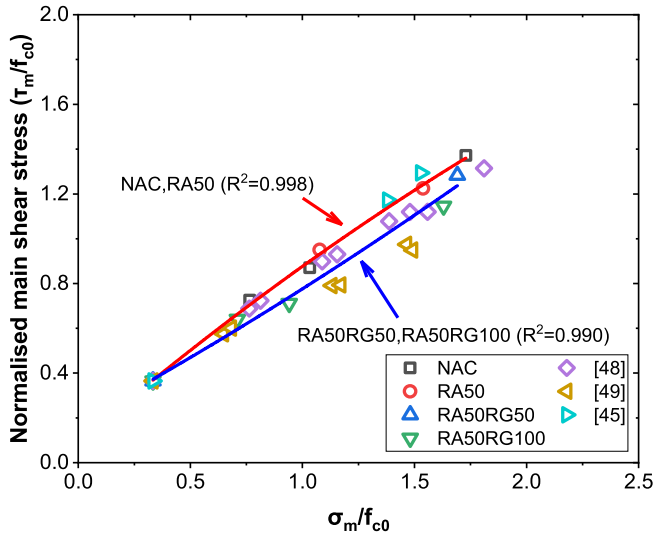

Fig. 19. Fitting performance of William-Warnke failure criterion under triaxial compression.

concrete has a nonlinear relationship with the increase rate of confining pressure, initially increasing rapidly and then slowing down (Jiang et al., 2023b).It can be expressed as:

$$\frac{f_c}{f_{c0}} = a_3\left(\frac{\sigma_c}{f_{c0}}\right)^{b_3} + 1 \tag{12}$$

where, a_3 and b_3 are parameters. f_c, f_{co} and σ_c are consistent with the symbols in Mohr-Coulomb failure criterion.

Based on test data in this study, the parameters were calibrated and Power-Law failure criteria for concrete specimens can be expressed as Eqs. (13) and (14).

$$\text{NAC and RA50}\ \frac{f_c}{f_{c0}} = 5.398\left(\frac{\sigma_c}{f_{c0}}\right)^{0.744} + 1 \tag{13}$$

$$\text{RA50RG50 and RA50RG100}\ \frac{f_c}{f_{c0}} = 4.979\left(\frac{\sigma_c}{f_{c0}}\right)^{0.959} + 1 \tag{14}$$

The Power-Law failure curves for concrete specimens with and without RGS was plotted in Fig. 20. In addition, existing data provided

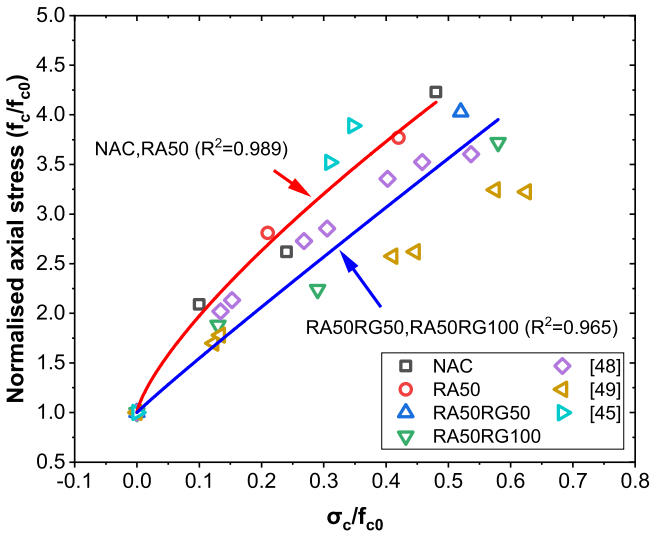

Fig. 20. Fitting performance of Power-Law failure criterion under triaxial compression.

by other researchers (Meng et al., 2017; Chen et al., 2019; Folino and Xargay, 2014) in triaxial compression experiments of RAC were presented together. The failure surfaces of NAC and RA50 satisfied the Power-Law failure criterion with the fitting correlation coefficient R^2 of 0.989, whereas the fitting curve of RA50RG50 and RA50RG100 were closer to a straight line.

A comprehensive comparison shows that the William-Warnke failure criterion had the best fitting performance on test data in this study. The fitting correlation coefficient R^2 for concrete specimens with and without RGS are both higher than 0.99. Moreover, the William-Warnke failure curve proposed from this experiment is closer to RAC triaxial compression data obtained by other researchers.

4.2. Failure criteria for triaxial compression with pore water pressure

At present, there is still a lack of test data on the triaxial compressive strength of concrete materials under a constant pore water pressure. This study drew on Mohr-Coulomb failure criterion and Power-Law failure criterion and proposed a new failure criterion model to describe the strength surface of RAC with and without RGS. The failure criterion can be expressed as:

$$f_c = k_4\sigma_p + b_4 \tag{15}$$

$$\frac{f_c}{f_{c0}} = a_5\left(\frac{\sigma_c}{f_{c0}}\right)^{b_5} + c_5 \tag{16}$$

Coefficients k_4, b_4, a_5, b_5 and c_5 can be calculated based on test data. The verified failure criteria are shown in Eqs. (17)–(20):

$$\text{NAC and RA50}\ f_c = -4.87\sigma_p + 4.02 \tag{17}$$

$$\text{NAC and RA50}\ f_c = -2.49\sigma_p + 3.96 \tag{18}$$

$$\text{RA50RG50 and RA50RG100}\ \frac{f_c}{f_{c0}} = -5.24\left(\frac{\sigma_c}{f_{c0}}\right)^{1.09} + 3.99 \tag{19}$$

$$\text{RA50RG50 and RA50RG100}\ \frac{f_c}{f_{c0}} = -3.35\left(\frac{\sigma_c}{f_{c0}}\right)^{1.46} + 3.89 \tag{20}$$

The verification of proposed failure criteria and test data of concrete specimens under triaxial compression with pore water pressure are shown in Fig. 21. It can be found that normalised axial stress of NAC and RA50 decreased faster than RA50RG50 and RA50RG100 with pore water pressure. The peak stress of NAC and RA50 was closer to a linear

relationship with normalised pore water pressure. The power function can achieve a better fitting result for RAC containing RGS, but the fitting correlation coefficient R^2 did not exceed 0.9.

5. Stress-strain model

The stress-strain behaviour of NAC and RAC under uniaxial and triaxial compression has been studied by many researchers (Xue et al., 2023b; Xu et al., 2021). Based on the test data, empirical models were proposed, including CEB-FIP model, Collins and Mitchell's model and Binici's model etc (Tang et al., 2019). However, to the authors' knowledge no model has been proven to predict the stress-strain trends of RAC with RGS under triaxial compression and pore water pressure. By comparing existing models, Collins and Mitchell's model in Eq. (21) (Collins and Mitchell, 1991), Guo and Zhang's model in Eq. (22) (Guo et al., 1982) and Chen's model in Eq. (23) (Chen et al., 2019) were selected to fit experimental data of uniaxial compression, triaxial compression and triaxial compression combined with pore water pressure respectively. From the analysis in Section 4, it can be known that RGS could change the internal friction angle of concrete specimens. Therefore, the concrete specimens were divided into two groups (concrete specimens with and without RGS), which are discussed in Section 5.1 and 5.2 respectively.

$$\text{Uniaxial compression } \frac{\sigma_a}{f_{c0}} = \begin{cases} \dfrac{A_1\left(\dfrac{\varepsilon_a}{\varepsilon_{ap0}}\right)}{A_1 - 1 + \left(\dfrac{\varepsilon_a}{\varepsilon_{ap0}}\right)^{A_1}} & 0 \le \dfrac{\varepsilon_a}{\varepsilon_{ap0}} < 1 \\ \dfrac{A_1\left(\dfrac{\varepsilon_a}{\varepsilon_{ap0}}\right)}{A_1 - 1 + \left(\dfrac{\varepsilon_a}{\varepsilon_{ap0}}\right)^{A_1 B_1}} & \dfrac{\varepsilon_a}{\varepsilon_{ap0}} \ge 1 \end{cases} \tag{21}$$

.

.

$$\text{Triaxial compression } \frac{\sigma_a}{f_c} = \begin{cases} A_2\left(\dfrac{\varepsilon_a}{\varepsilon_{ap}}\right) + (3 - 2A_2)\left(\dfrac{\varepsilon_a}{\varepsilon_{ap}}\right)^2 + (A_2 - 2)\left(\dfrac{\varepsilon_a}{\varepsilon_{ap}}\right)^3 & 0 \le \dfrac{\varepsilon_a}{\varepsilon_{ap}} < 1 \\ \dfrac{\left(\dfrac{\varepsilon_a}{\varepsilon_{ap}}\right)}{B_2\left(\dfrac{\varepsilon_a}{\varepsilon_{ap}} - 1\right)^2 + \left(\dfrac{\varepsilon_a}{\varepsilon_{ap}}\right)} & \dfrac{\varepsilon_a}{\varepsilon_{ap}} \ge 1 \end{cases} \tag{22}$$

$$\text{Pore water pressure } \frac{\sigma_a}{f_c} = \begin{cases} \dfrac{A_3\left(\dfrac{\varepsilon_a}{\varepsilon_{ap}}\right) - \left(\dfrac{\varepsilon_a}{\varepsilon_{ap}}\right)^2}{1 + (A_3 - 2)\left(\dfrac{\varepsilon_a}{\varepsilon_{ap}}\right)} & 0 \le \dfrac{\varepsilon_a}{\varepsilon_{ap}} < 1 \\ \dfrac{\dfrac{\varepsilon_a}{\varepsilon_{ap}}}{B_2\left(\dfrac{\varepsilon_a}{\varepsilon_{ap}} - 1\right)^2 + \left(\dfrac{\varepsilon_a}{\varepsilon_{ap}}\right)} & \dfrac{\varepsilon_a}{\varepsilon_{ap}} \ge 1 \end{cases} \tag{23}$$

.

5.1. NAC and RA50

Based on test data, A_1 and B_1 in Eq. (21) were calibrated as 3.52 and 1.05 respectively for NAC and RA50 under uniaxial compression. For NAC and RA50 under triaxial compression, the model Eq. (22) considered the ductility enhancement under the influence of confining pressure, which is shown on the stress-strain curve with a higher peak strain and a gentle descending part. The parameters A_2 and B_2 were determined as 3.52 and 0.25 respectively by regression analysis. The situation was even more special under triaxial compression combined with pore water pressure. This is shown by an increase in the elastic modulus and a decrease in the peak stress. Moreover, when the pore water pressure reached 13 MPa, the post-peak curve of the concrete specimen become steeper, close to the stress-strain curve under uniaxial compression. Traditional uniaxial and triaxial compression empirical models are not suitable for this situation. By comparison, Chen et al. (2019) proposed a model which was modified from CEB-FIP model (M. CE, 1990) and Guo and Zhang's model (Guo et al., 1982) for studying the mechanical properties of RAC can achieve a better prediction of stress-strain curves of concrete specimens under triaxial compression combined with pore water pressure. The parameters A_3 and B_3 for NAC and RA50 under triaxial compression with pore water pressure of 5 MPa and 9 MPa were determined as 9.69 and 0.11 respectively. When pore water pressure reached 13 MPa, A_3 and B_3 were 4.35 and 0.59 respectively.

The comparison of test data and above models is shown in Figs. 22–24. The empirical model selected in this study can achieve a satisfying predicting result for stress-strain development trends of NAC and RA50 under various stress states, especially in the rising part of the curves. Due to the multi-phase and heterogeneous nature of concrete materials, numerous accidental conditions may occur after cracks generated, and therefore, deviations between the prediction results and experimental data occurred in the descending part of the curve.

5.2. RA50RG50 and RA50RG100

The ductility of RAC containing RGS was better than ordinary NAC and RAC. As shown in Fig. 25, when uniaxial compression empirical model Eq. (21) was used to fit the experimental data, deformities appeared in the descending part of the curve. After switching to the triaxial compression model Eq. (22), the fitting curve returns to normal. However, there were still differences between the predicted results and the experimental data in the descending part of the curve. This may be related to the poor bonding performance between RGS and cement paste. The high porosity and weak cohesion strength in ITZ-Glass increased the discreteness of the data after the specimens damaged. For RA50RG50 and RA50RG100 under uniaxial compression, A_2 and B_2 in Eq. (22) were determined as 1.49 and 1.51 respectively. Under triaxial compression, the model Eq. (22) was still used to fit the experimental data. Parameters A_2 and B_2 were calibrated as 3.63 and 0.15 respectively for RA50RG50 and RA50RG100. The fitting curves and experimental data under triaxial compression were presented in Fig. 26. When concrete specimens were subjected to triaxial compression combined with

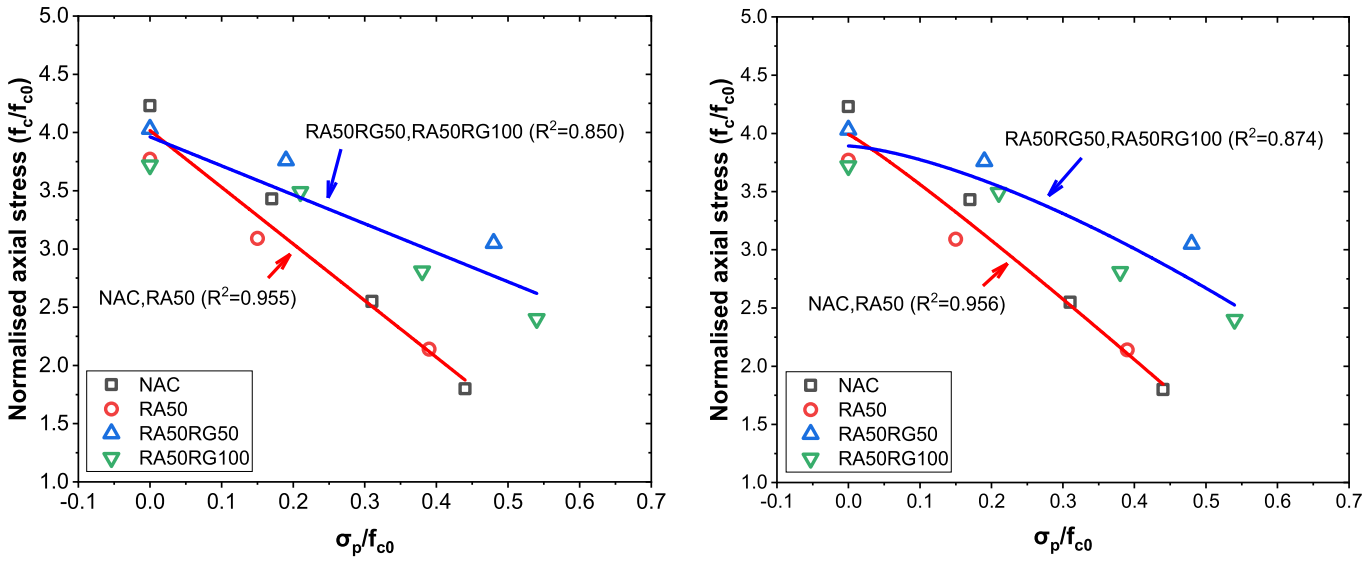

Fig. 21. Fitting performance under triaxial compression with pore water pressure.

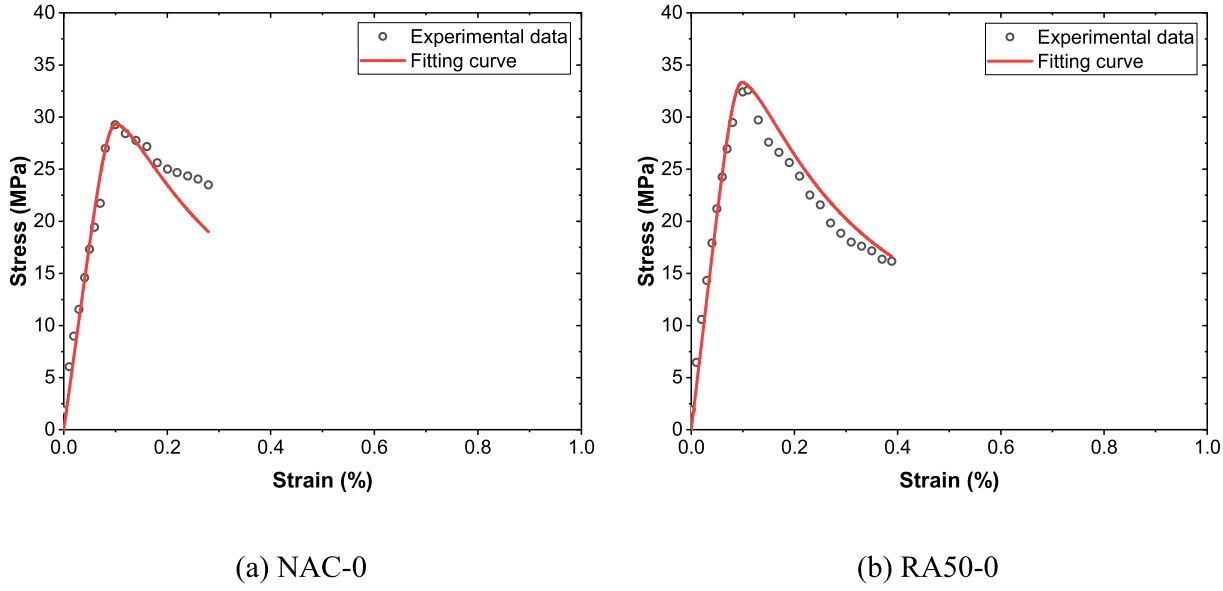

Fig. 22. Comparison of experimental results and fitting curves of NAC and RA50 under uniaxial compression.

pore water pressure of 5 MPa and 9 MPa, the parameters A_3 and B_3 in Eq. (23) were determined as 10.78 and 0.18. High pore water pressure improved the steepness of the descending part of the stress-strain curve. As a result, when pore water pressure rose to 14 MPa, A_3 and B_3 were 4.44 and 0.27 respectively. Similar to NAC and RA50, the empirical models had satisfying fitting performance for the rising part of stress-strain curves, but there were deviations in the descending part, as shown in Fig. 27.

6. Conclusions

Triaxial compressive properties of recycled concrete containing RCA and RGS under the effect of pore water pressure were analysed based on stress-strain curves. Nanoscratch and BSE-based image analysis were used to identify characteristics of ITZs. The results were used to explain the mechanism of the recycled concrete performance under various complex stress states. The following conclusions can be drawn as below.

(1) Nanoscratch is a more effective method for determining the ITZ width than traditional techniques, like nanoindentation and image analysis. In the study, the widths of New ITZ-RCA and ITZ-Glass were found the largest, at 27.91 μm and 30.77 μm respectively. ITZ-NCA, Old ITZ-RCA, and ITZ-NFA had smaller widths at around 10 μm.

(2) The microscopic properties of ITZ are not only related to the mixture ratio of cement paste, but also closely related to the chemical activity and specific surface area of aggregate. For coarse aggregate, the scratch hardness of New ITZ-RCA was higher than that of ITZ-NCA because the rough surface of the old mortar weakened the influence of 'wall effect', and the

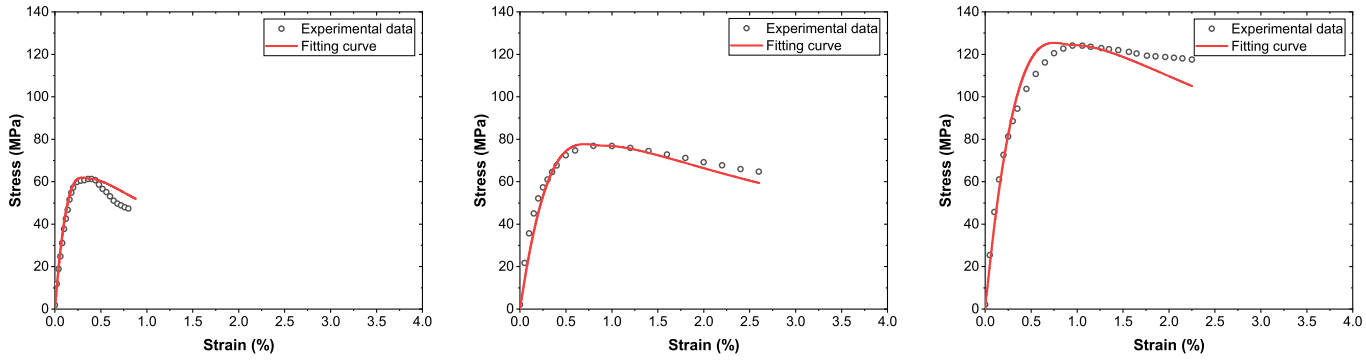

(a) NAC-3 (b) NAC-7 (c) NAC-14

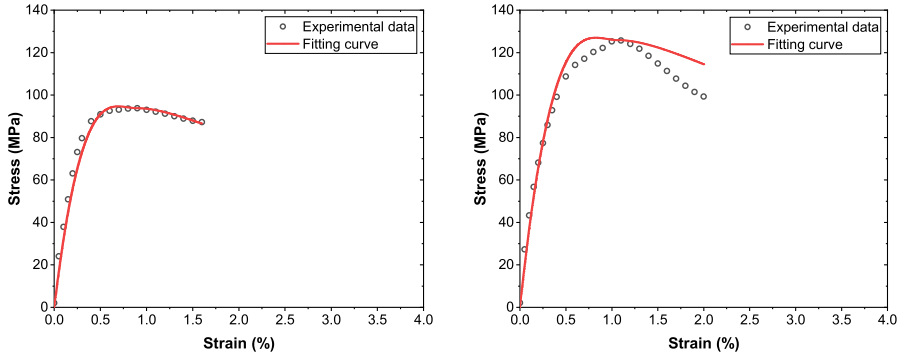

(d) RA50-7 (e) RA50-14

Fig. 23. Comparison of experimental results and fitting curves of NAC and RA50 under triaxial compression.

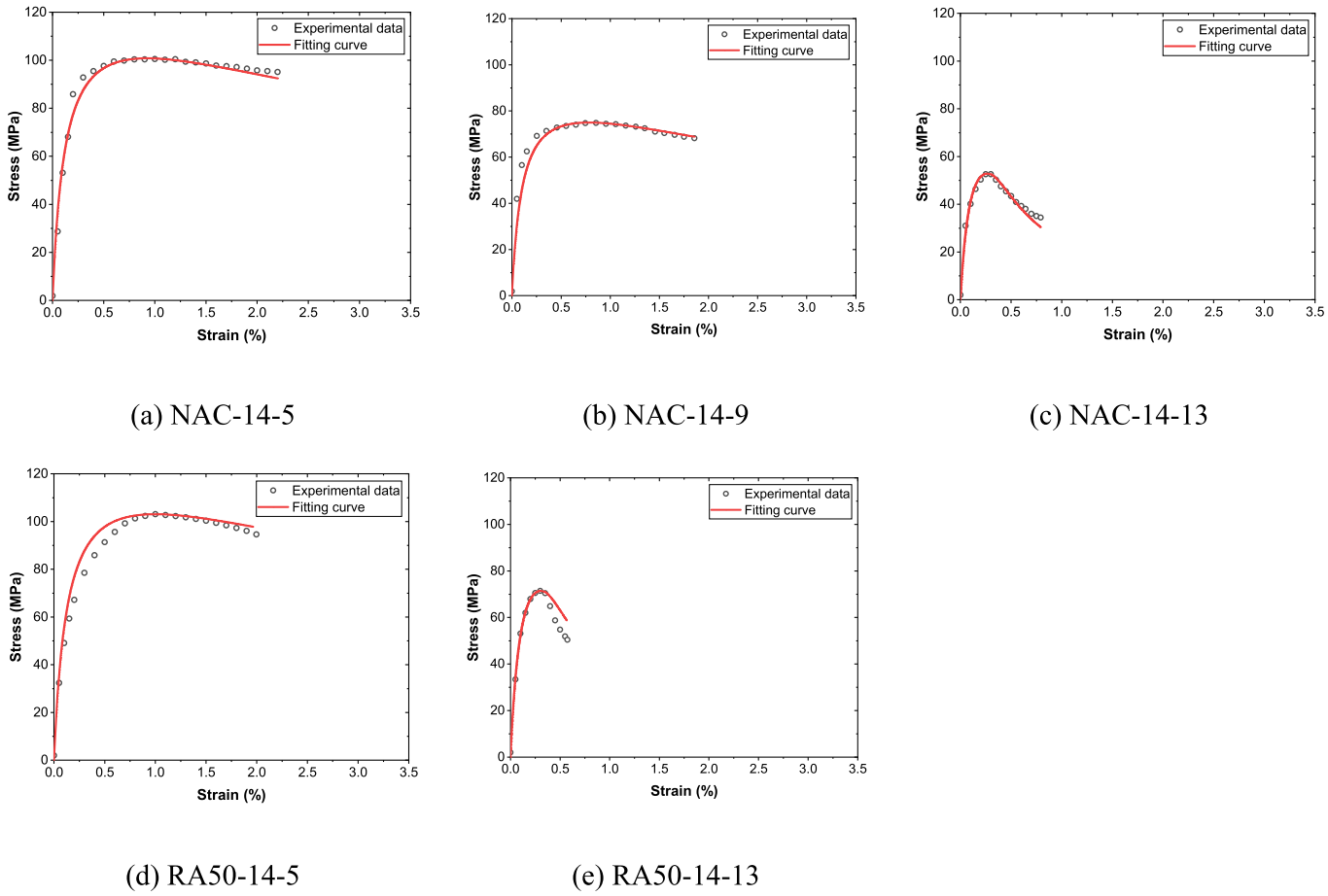

Fig. 24. Comparison of experimental results and fitting curves of NAC and RA50 under triaxial compression with pore water pressure.

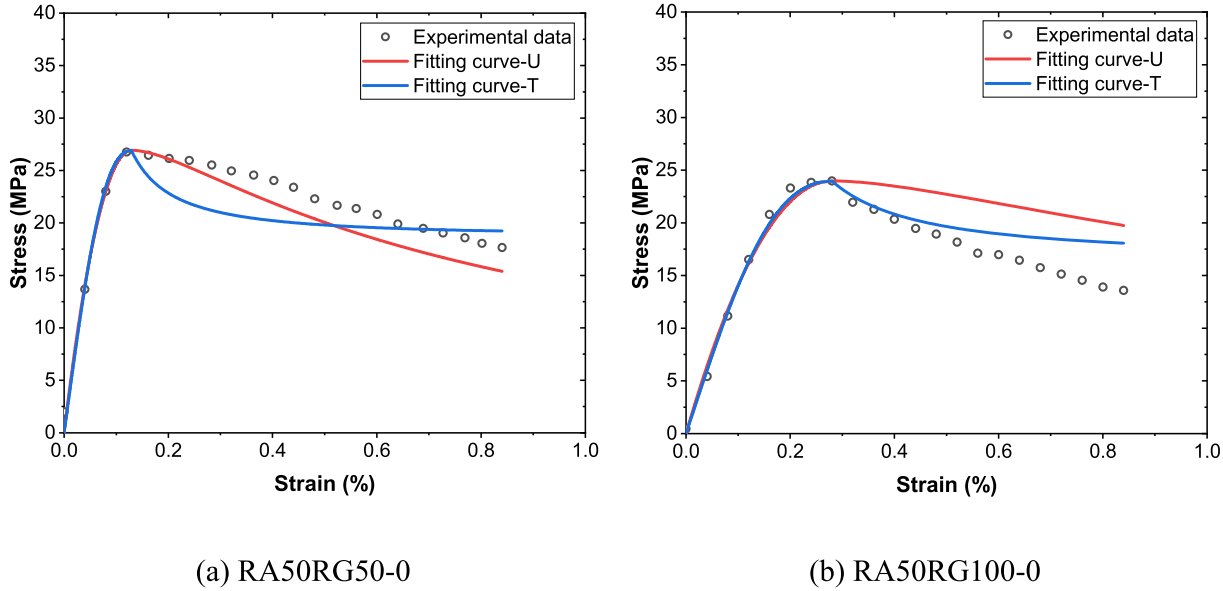

Fig. 25. Comparison of experimental data and fitting curves of RA50RG50 and RA50RG100 under uniaxial compression.

incompletely hydrated particles in the old mortar enhanced the cohesion with new ITZ. For fine aggregate, ITZ-Glass contained fewer unhydrated clinkers, less CH, and had a higher porosity, resulting in low scratch hardness.

(3) Under triaxial compression, the confining pressure significantly enhanced the peak stress, axial peak strain, and maximum volumetric strain of concrete specimens. When pore water pressure existed, the elastic modulus of RA50-14-13 and RA50RG100-14-13 improved by 69.6 % and 64.9 % respectively compared to

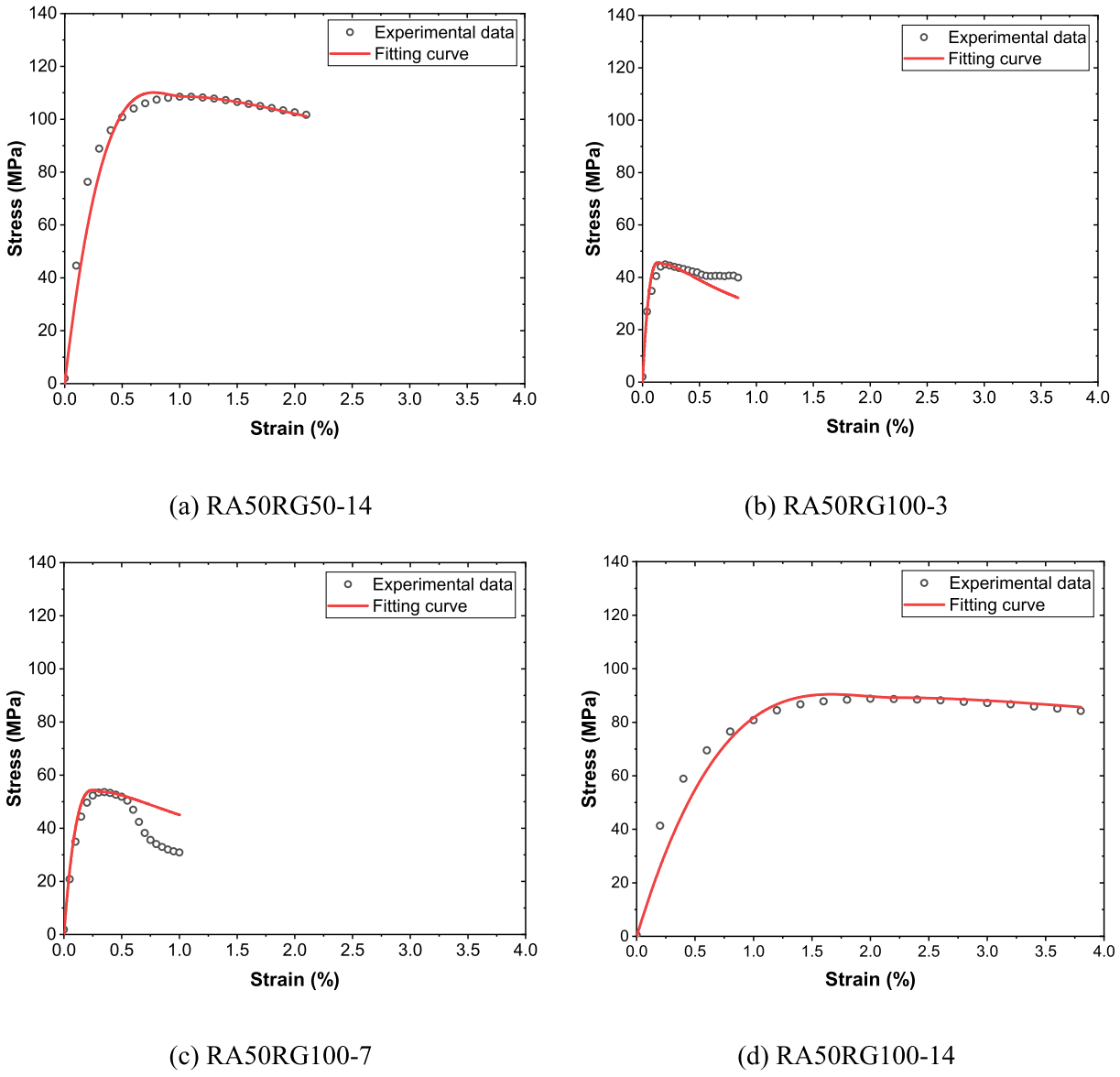

Fig. 26. Comparison on experimental data and fitting curves of RA50RG50 and RA50RG100 under triaxial compression.

their counterparts. However, the peak strain of RA50-14-13 and RA50RG100-14-13 reduced to 0.3 %–0.4 % due to the supporting effect of pore water pressure. Meanwhile, because of the promotion effect of pore water pressure on crack expansion, peak stress decreased by 24.3 %–57.4 when pore water pressure was 13 MPa, and the descending part of stress-strain curves became steeper.

(4) RCA would not weaken the mechanical properties of concrete specimens under triaxial compression and pore water pressure. However, when NFA was replaced by RGS, the peak stress decreased significantly from 33.35–125.87 MPa (RA50) to only 23.97–89.19 MPa (RA50RG100), and the peak strain improved under various stress states because of the porous ITZs. Numerous pores and low-density C–S–H within ITZ-Glass also provided space for compression deformation. When the confining pressure reached 14 MPa and pore water pressure was 0–5 MPa, RA50RG100 were destroyed in a compression state.

(5) RGS reduced the internal friction angle of concrete specimens because of the poor cohesion at glass-paste matrix interface. When analysing the failure surface of concrete specimens under triaxial compression with pore water pressure, the experimental data need to be divided into two groups based on RGS. The William-Warnke failure criterion is suitable for fitting the failure surface of sustainable concrete with RCA and RGS under triaxial compression. For triaxial compression combined with pore water pressure condition, power function can be used to describe the relationship between peak stress and normalised pore water pressure.

(6) Three empirical models were selected and used to predict the stress-strain curves of sustainable concrete under various stress states. High pore water pressure made the triaxial compressive stress-strain curves of the specimens behave more like that of the specimens under uniaxial compression. As a result, a modified uniaxial compression empirical model combined with triaxial compression model needs to be used. For stress-strain curves of specimens with RGS under uniaxial compression, a triaxial compression model achieved a better fitting performance, because RGS improved the ductility of concrete.

(7) The influence of pore water on the mechanical properties and durability of concrete structures is nonnegligible. The pore structure of sustainable concrete containing RCA and RGS is different from ordinary strength concrete. The permeability of

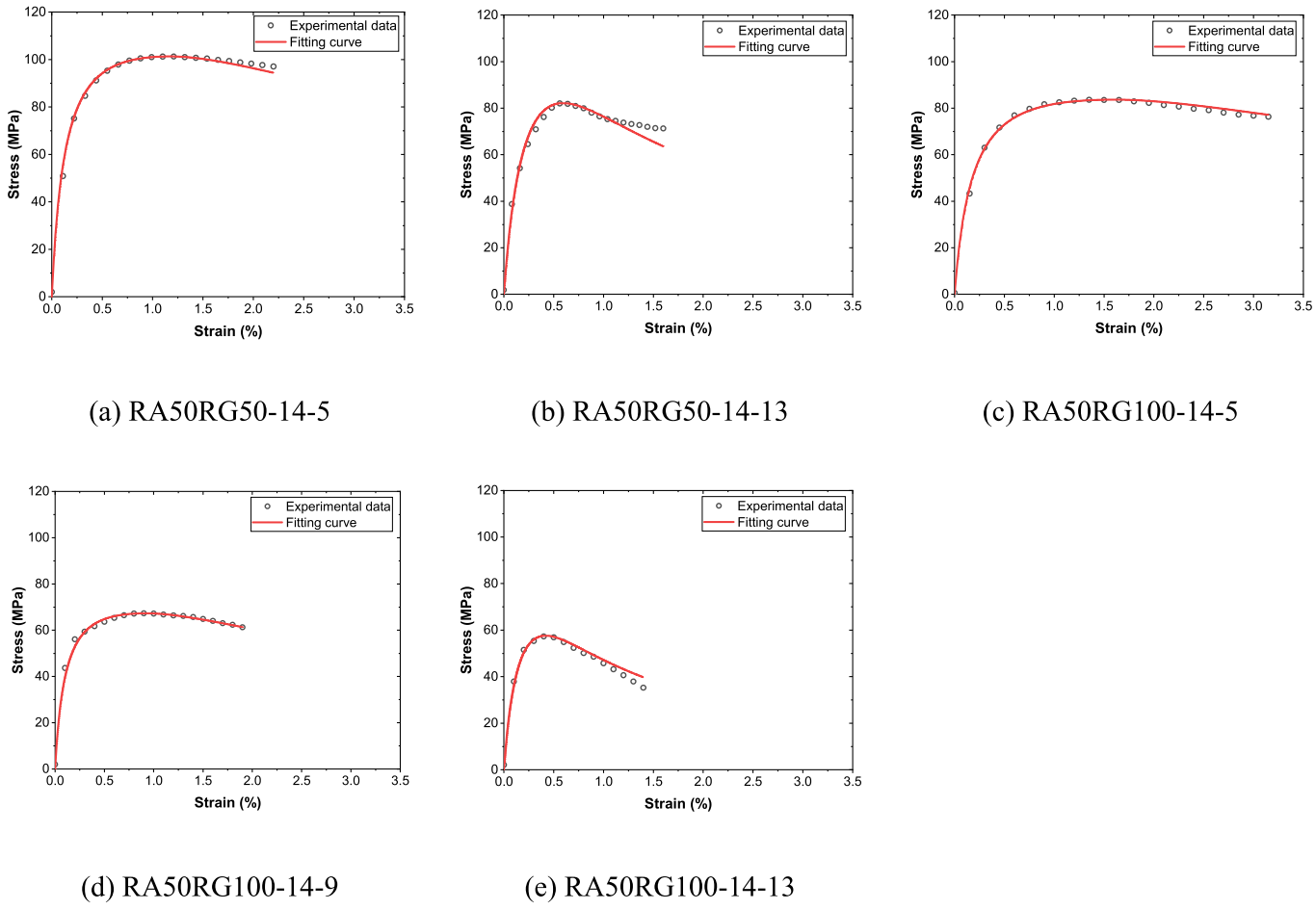

Fig. 27. Comparison of experimental data and fitting curves of RA50RG50 and RA50RG100 under triaxial compression with pore water pressure.

sustainable concrete when subjected to confining pressure can be investigated in the future. In addition, the influence of pore water pressure on the dynamic properties of concrete containing RCA and RGS also deserves attention.

CRediT authorship contribution statement

Hanbing Zhao: Formal analysis, Investigation, Methodology, Writing – original draft, Writing – review & editing. **Yong Hu:** Data curation, Validation, Writing – original draft, Writing – review & editing. **Yunan Li:** Data curation, Resources, Validation, Writing – original draft, Writing – review & editing. **Kejin Wang:** Formal analysis, Supervision, Validation, Writing – original draft, Writing – review & editing. **Frank Dehn:** Validation, Writing – original draft, Writing – review & editing. **Wengui Li:** Conceptualization, Funding acquisition, Supervision, Validation, Writing – original draft, Writing – review & editing.

Declaration of competing interest

The authors declare that they have no known competing financial interests or personal relationships that could have appeared to influence the work reported in this paper.

Data availability

Data will be made available on request.

Acknowledgements

All the authors appreciate the support from the Australian Research Council (ARC), Australia (FT220100177, LP230100288, DP220100036, DP220101051, IH200100010). The last author (Wengui Li) also thanks the International Excellence Fellowship of Karlsruhe Institute of Technology (KIT), Germany.

References

A. C33-18, 2018. Standard Specification for Concrete Aggregates.
A. G-171, 2017. Standard Test Method for Scratch Hardness of Materials Using a Diamond Stylus.
Bosque, I.F.S.d., Zhu, W., Howind, T., Matías, A., Rojas, M.I.S.d., Medina, C., 2017. Properties of interfacial transition zones (ITZs) in concrete containing recycled mixed aggregate. Cem. Concr. Compos. 81, 25–34.
Chen, K., Liu, Q., Chen, B., Zhang, S., Ferrara, L., Li, W., 2024. Effect of raw materials on the performance of 3D printing geopolymer: A review. J. Build. Eng. 84, 108501.
Chen, D., Yu, X., Shen, J., Liao, Y., Zhang, Y., 2017. Investigation of the curing time on the mechanical behavior of normal concrete under triaxial compression. Construct. Build. Mater. 147, 488–496.
Chen, Y., Chen, Z., Xu, J., Lui, E.M., Wu, B., 2019. Performance evaluation of recycled aggregate concrete under multiaxial compression. Construct. Build. Mater. 229, 116935.
Collins, M.P., Mitchell, D., 1991. Prestressed Concrete Structures. Prentice Hall, Englewood Cliffs, NJ.
Deng, Z., Wang, Y., Sheng, J., Hu, X., 2017. Strength and deformation of recycled aggregate concrete under triaxial compression. Construct. Build. Mater. 156, 1043–1052.
Diamond, S., Huang, J., 2001. The ITZ in concrete-a different view based on image analysis and SEM observations. Cem. Concr. Compos. 23, 179–188.
Djerbi, A., 2018. Effect of recycled coarse aggregate on the new interfacial transition zone concrete. Construct. Build. Mater. 190, 1023–1033.
Du, H., Tan, K.H., 2017. Properties of high volume glass powder concrete, Cem. Concr. Compos. 75, 22–29.

Folino, P., Xargay, H., 2014. Recycled aggregate concrete – mechanical behavior under uniaxial and triaxial compression. Construct. Build. Mater. 56, 21–31.
G.T. 14684, 2022. Sand for Construction (in Chinese).
G.T. 14685, 2022. Pebble and Crushed Stone for Construction (in Chinese).
G.T. 25176, 2010. Recycled Fine Aggregate for Concrete and Mortar (in Chinese).
G.T. 25177, 2010. Recycled Coarse Aggregate for Concrete (in Chinese).
Guo, Z., Zhang, X., Zhang, D., Wang, R., 1982. Experimental investigation of stress-strain curves for concrete, China. J. Build. Struct. 3 (1), 1–12.
Head, M.K., Buenfeld, N.R., 2006. Measurement of aggregate interfacial porosity in complex, multi-phase aggregate concrete: binary mask production using backscattered electron, and energy dispersive X-ray images. Cement Concr. Res. 36, 337–345.
Heukamp, F.H., Ulm, F.-J., Germaine, J.T., 2001. Mechanical properties of calcium-leached cement pastes triaxial stress states and the influence of the pore pressures. Cement Concr. Res. 31, 767–774.
Hoover, C.G., Ulm, F.J., 2015. Experimental chemo-mechanics of early-age fracture properties of cement paste. Cement Concr. Res. 75, 42–52.
Hosan, A., Shaikh, F.U.A., Sarker, P., Aslani, F., 2021. Nano- and micro-scale characterisation of interfacial transition zone (ITZ) of high volume slag and slag-fly ash blended concretes containing nano SiO2 and nano CaCO3. Construct. Build. Mater. 269, 121311.
Ismail, Z.Z., AL-Hashmi, E.A., 2009. Recycling of waste glass as a partial replacement for fine aggregate in concrete. Waste Manag. 29, 655–659.
Jiang, X., Xiao, R., Bai, Y., Huang, B., Ma, Y., 2022. Influence of waste glass powder as a supplementary cementitious material (SCM) on physical and mechanical properties of cement paste under high temperatures. J. Clean. Prod. 340, 130778.
Jiang, X., Zhu, H., Yan, Z., Zhang, F., Ye, F., Li, P., Zhang, X., Dai, Z., Bai, Y., Huang, B., 2023a. A state-of-art review on development and progress of backfill grouting materials for shield tunneling. Dev. Built Environ. 16, 100250.
Jiang, X., Li, Q., Yin, X., Xu, S., 2023b. Investigation on triaxial compressive mechanical properties of ultra high toughness cementitious composites with high strain capacity. Cement Concr. Res. 170, 107185.
Khedmati, M., Kim, Y.R., Turner, J.A., 2019. Investigation of the interphase between recycled aggregates and cementitious binding materials using integrated microstructuralnanomechanical-chemical characterization. Compos. B Eng. 158, 218–229.
Kim, Y., Hanif, A., Usman, M., Park, W., 2019. Influence of bonded mortar of recycled concrete aggregates on interfacial characteristics – porosity assessment based on pore segmentation from backscattered electron image analysis. Construct. Build. Mater. 212, 149–163.
Li, W., Xiao, J., Sun, Z., Kawashima, S., Shah, S.P., 2012. Interfacial transition zones in recycled aggregate concrete with different mixing approaches. Construct. Build. Mater. 35, 1045–1055.
Li, W., Luo, Z., Gan, Y., Wang, K., Shah, S.P., 2021. Nanoscratch on mechanical properties of interfacial transition zones (ITZs) in fly ash-based geopolymer composites. Compos. Sci. Technol. 214, 109001.
Lei, B., Yang, W., Guo, Y., Wang, X., Xiong, Q., Wang, K., Li, W., 2024. Interfacial adhesion between recycled aggregate and asphalt mastic filled with recycled concrete powder. Case Stud. Constr. Mater. 20, e02721.
Li, B., Dai, S., Zhan, Y., Xu, J., Guo, X., Yang, Y., Chen, Y., 2022. Strength criterion of recycled aggregate concrete under triaxial Compression: model calibration. Construct. Build. Mater. 320, 126210.
Li, C., Li, J., Ren, Q., Zheng, Q., Jiang, Z., 2023. Durability of concrete coupled with life cycle assessment: review and perspective. Cem. Concr. Compos. 139, 105041.
Li, Y., Zhao, H., Hu, Y., Qu, F., Zhu, D., Wang, K., Li, W., 2024. Effect of pore water pressure on mechanical performance of recycled aggregate concrete under triaxial compression. Cem. Concr. Compos. 146, 105402.
Lu, J., Yan, X., He, P., Poon, C.S., 2019. Sustainable design of pervious concrete using waste glass and recycled concrete aggregate. J. Clean. Prod. 234, 1102–1112.
Lu, J., Shen, P., Zheng, H., Zhan, B., Ali, H.A., He, P., Poon, C.S., 2020. Synergetic recycling of waste glass and recycled aggregates in cement mortars: physical, durability and microstructure performance. Cem. Concr. Compos. 113, 103632.
Luo, Z., Li, W., Wang, K., Shah, S.P., 2018. Research progress in advanced nanomechanical characterization of cementbased materials. Cem. Concr. Compos. 94, 277–295.
Luo, Z., Li, W., Tam, V.W.Y., Xiao, J., Shah, S.P., 2019. Current progress on nanotechnology application in recycled aggregate concrete. J. Sustain. Cem.-Based Mater. 8 (2), 79–96.
Luo, Z., Li, W., Wang, K., Castel, A., Shah, S.P., 2021. Comparison on the properties of ITZs in fly ash-based geopolymer and Portland cement concretes with equivalent flowability. Cement Concr. Res. 143, 106392.
Luo, Z., Li, W., Wang, K., Shah, S.P., Sheng, D., 2022. Nano/micromechanical characterisation and image analysis on the properties and heterogeneity of ITZs in geopolymer concrete. Cement Concr. Res. 152, 106677.
Lyu, K., She, W., Miao, C., Chang, H., Gu, Y., 2019a. Quantitative characterization of pore morphology in hardened cement paste via SEM-BSE image analysis. Construct. Build. Mater. 202, 589–602.
Lyu, K., Garboczi, E.J., She, W., Miao, C., 2019b. The effect of rough vs. smooth aggregate surfaces on the characteristics of the interfacial transition zone. Cem. Concr. Compos. 99, 49–61.
M. CE, 1990. Design of Concrete Structures. CEB-FIP Model Code.
Malecot, Y., Zingg, L., Briffaut, M., Baroth, J., 2019. Influence of free water on concrete triaxial behavior: the effect of porosity. Cement Concr. Res. 120, 207–216.
Meng, E., Yu, Y., Yuan, J., Qiao, K., Su, Y., 2017. Triaxial compressive strength experiment study of recycled aggregate concrete after high temperatures. Construct. Build. Mater. 155, 542–549.
Rangaraju, P.R., Olek, J., Diamond, S., 2010. An investigation into the influence of inter-aggregate spacing and the extent of the ITZ on properties of Portland cement concretes. Cement Concr. Res. 40, 1601–1608.
Scrivener, K.L., Crumbie, A.K., Laugesen, P., 2004. The interfacial transition zone (ITZ) between cement paste and aggregate in concrete. Interface Sci. 12, 411–421.
Sidorova, A., Vazquez-Ramonich, E., Barra-Bizinotto, M., Roa-Rovira, J.J., Jimenez-Pique, E., 2014. Study of the recycled aggregates nature's influence on the aggregate–cement paste interface and ITZ. Construct. Build. Mater. 68, 677–684.
Tang, Z., Hu, Y., Tam, V.W.Y., Li, W., 2019. Uniaxial compressive behaviors of fly ash/slag-based geopolymeric concrete with recycled aggregates. Cem. Concr. Compos. 104, 103375.
Tang, Z., Li, W., Tam, V.W.Y., Xue, C., 2020a. Advanced progress in recycling municipal and construction solid wastes for manufacturing sustainable construction materials. Resour. Conserv. Recycl. 6, 100036.
Tang, Z., Li, W., Tam, V.W.Y., Yan, L., 2020b. Mechanical performance of CFRP-confined sustainable geopolymeric recycled concrete under axial compression. Eng. Struct. 224, 111246.
Vargas, P., Restrepo-Baena, O., Tobón, J.I., 2017. Microstructural analysis of interfacial transition zone (ITZ) and its impact on the compressive strength of lightweight concretes. Construct. Build. Mater. 137, 381–389.
Vu, X.H., Malecot, Y., Daudeville, L., Buzaud, E., 2009. Experimental analysis of concrete behavior under high confinement: effect of the saturation ratio. Int. J. Solid Struct. 46, 1105–1120.
Vu, X.D., Briffaut, M., Malecot, Y., Daudeville, L., Ciree, B., 2015. Influence of the saturation ratio on concrete behavior under triaxial compressive loading. Sci. Technol. Nucl. Install., 976387
Wang, Y., Wang, Y., Zhao, Y., Li, G., Lyu, Y., Li, H., 2020. Experimental study on ultra-high performance concrete under triaxial compression. Construct. Build. Mater. 263, 120255.
Wang, B., Yan, L., Fu, Q., Kasal, B., 2021. A comprehensive review on recycled aggregate and recycled aggregate concrete. Resour. Conserv. Recycl. 171, 105565.
Wei, Y., Kong, W., Wang, Y., Sha, A., 2021. Multifunctional application of nanoscratch technique to characterize cementitious materials. Cement Concr. Res. 140, 106318.
Wong, H.S., Buenfeld, N.R., 2006. Euclidean Distance Mapping for computing microstructural gradients at interfaces in composite materials. Cement Concr. Res. 36, 1091–1097.
Wong, H.S., Buenfeld, N.R., 2009. Determining the water–cement ratio, cement content, water content and degree of hydration of hardened cement paste: method development and validation on paste samples. Cement Concr. Res. 39, 957–965.
Wong, H.S., Head, M.K., Buenfeld, N.R., 2006. Pore segmentation of cement-based materials from backscattered electron images. Cement Concr. Res. 36, 1083–1090.
Wu, K., Luo, S., Zheng, J., Yan, J., Xiao, J., 2022. Influence of carbonation treatment on the properties of multiple interface transition zones and recycled aggregate concrete. Cem. Concr. Compos. 127, 104402.
Wu, Y., Liu, C., Bai, G., Liu, H., Meng, Y., Wang, Z., 2023. 3D printed concrete with recycled sand: pore structures and triaxial compression properties. Cem. Concr. Compos. 139, 105048.
Xiao, J., Li, W., Sun, Z., Lange, D.A., Shah, S.P., 2013. Properties of interfacial transition zones in recycled aggregate concrete tested by nanoindentation. Cem. Concr. Compos. 37, 276–292.
Xu, Z., Li, J., Wu, P., Wu, C., 2021. Experimental investigation of triaxial strength of ultra-high performance concrete after exposure to elevated temperature. Construct. Build. Mater. 295, 123689.
Xue, W., Xu, L., Wang, Z., Min, T., Xu, J., 2023a. Experimental study on seepage evolution and microscopic characteristics of initially damaged concrete under variable confining pressure. Construct. Build. Mater. 393, 132157.
Xue, H., Zhu, H., Guo, M., Shao, S., Zhang, S., Zhang, Y., 2023b. Modeling for predicting triaxial mechanical properties of recycled aggregate concrete considering the recycled aggregate replacement. Construct. Build. Mater. 368, 130447.
Yang, Y., Wu, C., Liu, Z., Zhang, H., 2022. 3D-printing ultra-high performance fiber-reinforced concrete under triaxial confining loads. Addit. Manuf. 50, 102568.
Ye, T., Xiao, J., Zhao, W., Duan, Z., Xu, Y., 2022. Combined use of recycled concrete aggregate and glass cullet in mortar: strength, alkali expansion and chemical compositions. J. Build. Eng. 55, 104721.
Yue, G., Ma, Z., Liu, M., Liang, C., Ba, G., 2020. Damage behavior of the multiple ITZs in recycled aggregate concrete subjected to aggressive ion environment. Construct. Build. Mater. 245, 118419.
Zhang, W., Wang, S., Zhao, P., Lu, L., Cheng, X., 2019. Effect of the optimized triple mixing method on the ITZ microstructure and performance of recycled aggregate concrete. Construct. Build. Mater. 203, 601–607.
Zhang, Y., Zhang, S., Jiang, X., Zhao, W., Wang, Y., Zhu, P., Yan, Z., Zhu, H., 2023. Uniaxial tensile properties of multi-scale fiber reinforced rubberized concrete after exposure to elevated temperatures. J. Clean. Prod. 389, 136068.
Zhao, H., Li, W., Gan, Y., Mahmood, A.H., Zhao, X., Wang, K., 2024. Nano- and microscopic investigation on the strengthening mechanism of ITZs using waste glass powder in modeled aggregate concrete. J. Mater. Civ. Eng. 36 (4), 04024007.